



# Genesis of the sediment-hosted Haerdaban Zn-Pb deposit, Western Tianshan, NW China: Constraints from textural, compositional and sulfur isotope variations of sulfides

Zongsheng Jiang<sup>a,\*</sup>, Zuoheng Zhang<sup>b</sup>, Shigang Duan<sup>a</sup>, Chengshuai Lv<sup>c</sup>, Zhihui Dai<sup>d</sup>

<sup>a</sup> MNR Key Laboratory of Metallogeny and Mineral Assessment, Institute of Mineral Resources, Chinese Academy of Geological Sciences, Beijing 100037, China

<sup>b</sup> Institute of Geophysical and Geochemical Exploration, Chinese Academy of Geological Sciences, Langfang 065000, China

<sup>c</sup> School of the Earth Sciences and Resources, China University of Geosciences, Beijing 100083, China

<sup>d</sup> State Key Laboratory of Ore Deposit Geochemistry, Institute of Geochemistry, Chinese Academy of Sciences, Guiyang 550081, China

## ARTICLE INFO

### Keywords:

Sulfur isotope  
Trace element  
LA-ICP-MS  
Haerdaban Pb-Zn deposit  
Western Tianshan

## ABSTRACT

The sediment-hosted Haerdaban Zn-Pb deposit is a newly discovered Zn-Pb deposit in the Sailimu terrane, Western Tianshan (NW China), containing ca. 0.64 Mt of ore at 6.19 wt% Zn and 1.09 wt% Pb. The mineralization consists mainly of veins, breccias and semi-massive sulfide ores within the dolomitic limestone and calcareous slate. Using LA-ICP-MS, this study investigates trace element and sulfur isotope composition of sulfide to constrain the genesis of the deposit. Four pyrite types were identified by variations in texture and composition. Porous pyrite (Py1) shows a significant enrichment in Mn, Ag, Sb, Tl, Ba, Pb, Cu, and Zn, whereas the pyrite overgrowth (Py2) and euhedral pyrite (Py3) are enriched in Co and As, but depleted in all other trace elements. This compositional trend is attributed to the release of trace elements from pyrite during recrystallization from a porous to massive texture. Pyrite (Py4) associated with sphalerite is inclusion-rich, but exhibits a depletion in most trace elements, except Ni and Sb. The underlying carbonaceous sediments are interpreted as a source of Ni, Sb and other metals for the ore-forming fluids. Sphalerite displays a wide variety of colors from dark brown to pale yellow, primarily related to variations in Fe contents. The overall Fe contents (0.25 to 6.12 wt%), Cd contents (524 to 1875 ppm) and Zn/Cd ratios (320 to 1258) in sphalerite are compatible with those of SEDEX Zn-Pb deposit. The contents of other elements in sphalerite are generally low. Calculated temperatures using trace element contents in sphalerite (GGIMFis geothermometer) range from 163 °C to 309 °C, indicating progressive cooling of ore-forming fluid. Pyrite, sphalerite and galena display a wide range of  $\delta^{34}\text{S}$  values from +3.9 to +18.3‰. The association of lower positive  $\delta^{34}\text{S}$  values (+3.9 to +8.8‰) and epithermal suite elements (Ni, As, Sb, and Tl) enrichment in porous pyrite indicate that sulfur in early sulfides was derived from thermochemical sulfate reduction (TSR) with a possible magmatic input. The dominant population of heavier  $\delta^{34}\text{S}$  values (+13.8 to +18.3‰) of massive sulfide support TSR as the main source of sulfur. The intermediate  $\delta^{34}\text{S}$  values (+7.0 to +13.0‰) of vein sulfide are likely a mixing of TSR-derived sulfur with light sulfur leached from diagenetic pyrite. The current data support the classification of Haerdaban as a metamorphosed SEDEX Zn-Pb deposit, where the main mineralization was the product of remobilization and upgrading of early exhalative ores during hydrothermal events.

## 1. Introduction

Sediment-hosted Pb-Zn deposits represent the world's largest accumulations of base metals (Goodfellow and Lydon, 2007; Wilkinson, 2014). These deposit types typically include sedimentary exhalative (SEDEX) deposits in clastic-dominated sedimentary sequences and

Mississippi Valley-type (MVT) in carbonate-dominated platform sequences (Leach et al., 2010). Although it is widely accepted that these deposits formed mainly from sedimentary brines derived from evaporated seawater (e.g., Leach et al., 2010), a variety of ore-forming processes have been proposed for ore formation. Some SEDEX ores were suggested to have formed by exhalative processes on the basin floor (e.

\* Corresponding author at: Institute of Mineral Resources, Chinese Academy of Geological Sciences, Beijing 100037, China.

E-mail address: [jzongsheng@126.com](mailto:jzongsheng@126.com) (Z. Jiang).

<https://doi.org/10.1016/j.oregeorev.2021.104527>

Received 7 May 2021; Received in revised form 10 September 2021; Accepted 12 October 2021

Available online 21 October 2021

0169-1368/© 2021 The Authors.

Published by Elsevier B.V. This is an open access article under the CC BY-NC-ND license

(<http://creativecommons.org/licenses/by-nc-nd/4.0/>).

g., Goodfellow and Lydon, 2007; Large et al., 2002; Rajabi et al., 2015), whereas others would have formed by seafloor replacement during sedimentation or very early diagenesis (e.g., Kelley et al., 2004; Leach et al., 2005, 2010; Slack et al., 2004; Gadd et al., 2016). Determining the source of sulfur and ore-forming fluid responsible for mineralization is fundamental to understanding the genesis of the sediment-hosted Pb-Zn deposits, especially where both sedimentary-diagenetic and hydrothermal processes were involved in the complex mineralization history. Such information can be obtained from systematic studies on the variations in texture, trace element and sulfur isotope composition of sulfide, particularly when using laser ablation-inductively coupled plasma-mass spectrometry (LA-ICP-MS), which allows in situ analysis of sulfide minerals within their textural context (e.g., Kelley et al., 2004; Large et al., 2013; Cook et al., 2009; Qiu et al., 2018; Xie et al., 2018).

The Tianshan orogenic belt, in the southwestern part of the Central Asian Orogenic Belt (Xiao et al., 2008), is host to numerous porphyry Cu-Au, epithermal Au and sediment-hosted Zn-Pb (-Ag) deposits (e.g., Yakubchuk et al., 2005; Seltmann et al., 2013). The latter include the giant Tekeli, Koksū-Suuktyube, and Usek deposits in Kazakhstan (Seltmann et al., 2013) and the recently discovered Haerdaban, Tuokesai, and Sitaihaiquan deposits in NW China (Fig. 1; Table 1; Man, 2020; Xue et al., 2014). These deposits are hosted within the Proterozoic carbonate-clastic sediments along the northern margin of the Kazakhstan-Yili Block and have been moderately metamorphosed during the Paleozoic accretionary orogenesis. The genesis of these metamorphosed sediment-hosted Zn-Pb deposit remains ambiguous due to the complex structures and textures of ores. For the Tekeli deposit, Trofimova et al. (1978) proposed that the pyrite ores were related to sedimentary-diagenetic process, whereas the Zn-Pb ores were mainly formed by hydrothermal reworking and redeposition of earlier ores. Based on the geological characteristics, geochemistry and Si-S-Pb isotopes, the Tuokesai deposit has been considered by most workers to be a SEDEX deposit that formed by exhalative processes (Liu, 2015; Man, 2020; Man et al., 2020; Zhao, 2020). Unlike the Tuokesai deposit, which is dominated by laminated ores, vein and breccia ores are evidence for widespread hydrothermal activity at Haerdaban. Duan (2011) suggested a SEDEX model for the formation of Haerdaban, whereas Cheng et al. (2015) and Man (2020) favored an initial exhalative origin with a subsequent hydrothermal overprint. Until now, only limited sulfur isotope data for bulk sulfide separates are available (Cheng et al., 2015; Duan, 2011; Man, 2020), which may ignore the textural complexity and multistage growth of sulfide. There are still knowledge gaps regarding the source of sulfur and evolution of mineralization in the Haerdaban

deposit.

In this study, we present trace element and sulfur isotope data for sulfide from the Haerdaban Zn-Pb deposit using in situ LA-ICP-MS analyses. The aims of this paper are to (1) provide a detailed description of the different sulfide textures found within the deposit and interpretation on the processes by which sulfide formed; (2) use the texturally controlled trace element and sulfur isotope data to establish the potential sources of sulfur and the evolution of ore-forming fluids during mineralization; and (3) combine the textural observations and in situ geochemical data to gain a better understanding of the genesis of the deposit.

## 2. Regional geology

The Tianshan Orogen is located in the southwest part of the Central Asian Orogenic Belt (CAOB; Xiao et al., 2008), extending for approximately 2500 km from Uzbekistan to western China. It is an accretionary orogenic belt that was produced by closure of Paleozoic oceans and associated amalgamation of tectonic terranes during the late Paleozoic to early Mesozoic (Allen et al., 1992; Gao et al., 1998; Windley et al., 2007; Xiao et al., 2008). The Sailimu Terrane (NW China) is one of the Precambrian microcontinental fragments that was involved in the accretionary orogenesis of the Tianshan Orogen (Windley et al., 2007; Biske and Seltmann, 2010). It is located along the north margin of the Western Tianshan in China, bounded by the Bortala River Fault to the north and the North Borohoro Mountain Fault to the south (Fig. 1; Li and Qin, 1989; Gu et al., 2014). The structural framework of Sailimu Terrane is dominated by E-W to SE-NW-trending chains of folds and faults, which are subparallel to the main shear zone boundaries of the Sailimu Terrane.

The Precambrian basement in the Sailimu Terrane is characterized by metamorphosed quartzite-schist, granitoid, clastic-carbonate and coarse clastic assemblages, similar to the lithologies of the adjacent Tekeli domain in Kazakhstan (Fig. 1; Degtyarev et al., 2017; Wang et al., 2014). The oldest exposed rocks in the Sailimu Terrane are quartzites, quartz-mica to micaceous schist and paragneiss with marble lenses of the Wenquan Group, which was previously considered as Paleoproterozoic in age (XBGMR, 1993). Recent U-Pb data revealed two age populations of 1370–1600 Ma and 880–950 Ma for detrital zircons from schist rock and age of 926–845 Ma for augen granite-gneiss and leucocratic granite of the Wenquan Group (Hu et al., 2010; Wang et al., 2014). To the south, Mesoproterozoic clastic-carbonate rocks mostly occur around the Sailimu Lake, consisting of slate, phyllite, marble and

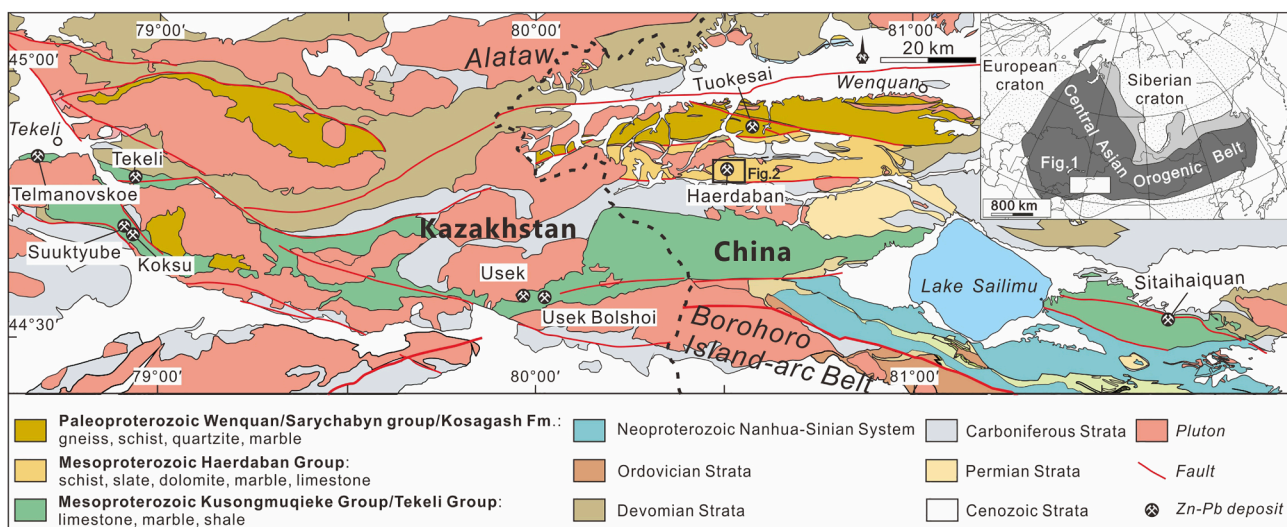


Fig. 1. Geological map of the Tekeli-Sailimu terrane showing the major sediment-hosted Zn-Pb deposits (simplified from unpublished geological map). Inset map shows location of the Tekeli-Sailimu terrane in the Central Asian Orogenic Belt (modified from Sengör et al., 1993).

**Table 1**  
Main characteristics of selected Zn-Pb deposits in the Sailimu and Tekeli Zn-Pb belt.

Deposit	Country (district)	location coordinate	Resource	Geological setting	Age of host strata	Host rock	Orebody geometry	Mineralization textures, style	Ore minerals	Gangue minerals	Selected references
Haerdaban	China (Xinjiang)	80°32'44"E, 44°48'38"N	0.64 Mt@6.19 % Zn and 1.09 % Pb, Zn/Pb ratio = 5:1	NE margin of the Kazakhstan-Yili block	Neoproterozoic	Dolomitic limestone and calcareous slate of the Haerdaban Group	Stratified and lenticular	Disseminated, breccia vein, massive to semi-massive	Sphalerite, galena, pyrite, with minor pyrrhotite	Dolomite, ankerite, quartz, calcite, and minor barite, siderite, chlorite, sericite	Cheng et al., 2015; Zhu et al., 2015; This study
Tuokesai	China (Xinjiang)	80°34'45"E, 44°52'30"N	.	NE margin of the Kazakhstan-Yili block	Neoproterozoic	Marble of the Wenquan Group	Stratified and lenticular	Laminated, disseminated	Sphalerite, galena, pyrite, with minor pyrrhotite	Calcite, quartz, and minor dolomite	Cheng et al., 2011; Man et al., 2020
Sitaihaiquan	China (Xinjiang)	81°43'00"E, 44°32'30"N	0.62 Mt@1 to 10.6 % Zn and 0.02 to 2.83 % Pb	NE margin of the Kazakhstan-Yili block	Neoproterozoic	Limestone of the Kusongmuqieke Group	Stratified, lenticular and vein	Veinlet stockwork, vein, breccia and disseminated	Smithsonite, with minor sphalerite, galena and pyrite	Calcite, minor quartz and dolomite	Man, 2020
Tekeli	Kazakhstan (Tekeli)	78°55'50"E, 44°46'45"N	5 Mt@4.19% Zn, 2.8% Pb and 42.6 g/t Ag, Zn/Pb ratio = 2:1	NE margin of the Kazakhstan-Yili block	Vendian-Cambrian?	Limestone, coal, clay and siliceous-clayey shale of the Tekeli Suite	Lenticular and tabular	Laminated, disseminated (primary ores); breccia, massive (metamorphosed ores)	Sphalerite, galena, pyrite, pyrrhotite, tetrahedrite, tennantite	Quartz, calcite, dolomite, sericite, shungite, chlorite	Xue et al., 2017; Man et al., 2020

limestone of Haerdaban group (Changcheng System), and schistose, bedded or massif limestone of Kusongmuqieke group (Jixian System) (XBGM, 1993). Farther to the southeast, Neoproterozoic rocks are composed of stromatolite-bearing dolomitic limestone and marble of Kaiertasi group (Qingbaikou System), and succession of basal conglomerate, massive basalt, sandstone, conglomerate and siltstone with rare limestone layers, tilloid horizons of the Nanhua-Sinian (ca. 640 Ma) Kailaketi Group (Wang et al., 2014; He et al., 2015).

Precambrian lithologies in the Sailimu Terrane are unconformably overlain by or in fault contact with Paleozoic strata. Early Paleozoic rocks occur only in the southeast of the Sailimu Lake, consisting of Cambrian phosphoritic sandstone, phosphorite, limestone and siltstone with chert layers (Wang et al., 2014; He et al., 2015), Ordovician pelitic slate, shale, chert, limestone and siltstone, and Silurian limestone, clastic rocks and calc-alkaline volcanic rocks (XBGM, 1993; Gao et al., 1998). The Late Paleozoic sequence is composed of Carboniferous volcano-sedimentary series and associated plutonic rocks, and Permian terrigenous rocks associated with sporadically distributed felsic magmatic rocks (XBGM, 1993)

Two dominant types of mineralization occur in the region and include: stratiform Zn-Pb deposit and porphyry/skarn Cu-Au-Mo deposit. Sediment-hosted Zn-Pb deposits and occurrences mostly occur in dolomite, dolomitic limestone and siliceous rock of the Wenquan group and Haerdaban group, e.g., the Haerdaban, Tuokesai, and Sitaihaiquan deposits, constituting the Sailimu Zn-Pb belt (Table 1; Xue et al., 2014). These deposits share many geological and mineralogical similarities with the world-class Tekeli and Koksuu-Suuktuube, Usek deposits in Kazakhstan (Xue et al., 2014). The Sailimu Zn-Pb belt has therefore been interpreted to represent the eastern continuation of the Tekeli Zn-Pb belt (Xue et al., 2014; Man et al., 2020), confirming the high potential for economic Zn-Pb mineralization in the basement rocks of the Tianshan belt. During accretionary orogenesis of the Western Tianshan, porphyry-style and skarn Cu-Au-Mo mineralization are commonly associated with the Late Paleozoic granodioritic stocks and sills, and their country rocks, e.g., the Lamasu, Kekesai, and Dabate deposits (Liu et al., 2018; Han et al., 2020).

### 3. Deposit geology

The Haerdaban deposit is located in the western corner of the Sailimu Terrane, approximately 40 km southwest of the town of Wenquan (Fig. 1). It was discovered during the investigation of Zn-Pb anomalies by the Xinjiang Institute of Geological Exploration for Nonferrous Resources (XIGENR) in 2007. Subsequent exploration work by XIGENR has defined a total indicated and inferred resource of 0.64 million tonnes (Mt) with grades of 6.19 wt% Zn and 1.09 wt% Pb (Zhu et al., 2015). The mineral deposit remains undeveloped.

The deposit lies on the southern limb of the regional Haerdaban syncline in which clastic-carbonate strata and stratabound sulfide lenses are EW-trending, 70° to 87° S-dipping. The lithostratigraphy of the deposit is dominated by the Haerdaban Group, which is divided into two different subgroups, the lower Subgroup and the upper Subgroup. The lower Haerdaban Subgroup in the northern part of the district consists of biotite schist, sericite schist, and thin bedded silty limestone. Toward the south, the 40- to 60-m-thick marble layer marks the transition from the lower Subgroup to the upper Subgroup, which contains silty limestone, dolomitic limestone, dolomite, carbonaceous micritic limestone, siliceous rock, and calcareous slate. To the south, the Haerdaban Group is in fault contact with the Lower Carboniferous Aqialehe Formation, a shallow marine unit that is composed of lithic sandstone, siltstone, conglomerate with bedded limestone lenses. Paleozoic granodiorite and diorite porphyry sills and dikes were emplaced in the district, and some of these intrusions are spatially associated with Zn-Pb mineralization. However, it is uncertain whether these intrusions were genetically related to the sulfide mineralization.

The Zn-Pb sulfide mineralization is restricted in the dolomitic

limestone and calcareous slates of the upper Haerdaban Subgroup to a 500- to 800-m-wide and 6000-m-long zone (Fig. 2a). Drilling program in 2014 identified a total indicated and inferred resources of 8.2 million tonnes (Mt) with grades of 6.19 wt% Zn and 1.09 wt% Pb (Zhu et al., 2015). The orebodies consist of a stacked series of stratabound lenses that strike mainly E-W and dip steeply to the south (70°–85°). They are grouped into three principal mineralized zones, the Zone I, Zone II, and Zone III (Fig. 2a). The Zone I includes 22 orebodies that consist of vein to

massive sulfide ores and contain ~83% of the total ore reserves of the deposit. The main lenses are defined over a strike length of more than 500 m and a vertical extent of over 300 m with a thickness up to 23.26 m, and remain open at depth and along strike (Fig. 2b, c; Cheng et al., 2015; Zhu et al., 2015). The sulfide lenses are normally enveloped by carbonate alteration zones, which are characterized by dolomite–ankerite–calcite–(quartz) veins and cements in the dolomitic siltstones and the polymictic breccias.

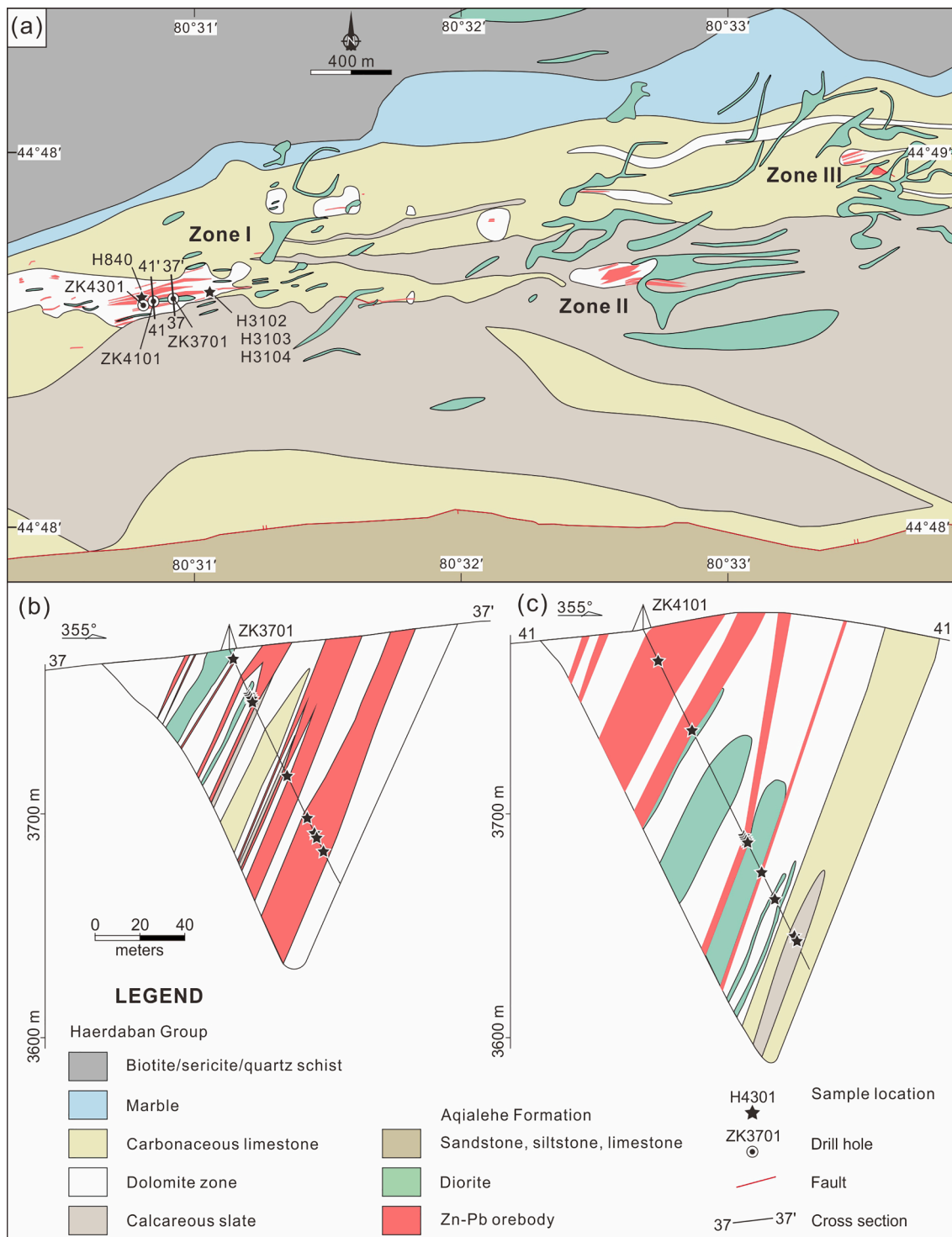


Fig. 2. (a) Geologic map of the Haerdaban Zn-Pb deposit showing the locations of studied drill cores and surface samples. (b, c) Cross sections through the Zone I along line 37-37' and line 41-41', showing the ore lenses and surrounding lithologies. Rock types and contacts are based on surface mapping and drilling. Locations of drill core samples are labeled. All figures modified from Zhu et al. (2015).



The mineralization is present as massive sulfides, veins, breccias, and disseminated ores that record a texturally complex history of ore emplacement (Fig. 3). Disseminated ore comprises low-grade occurrences of Zn, and is commonly overgrown by vein with coarse-grained sphalerite-dolomite assemblage (Fig. 3a, b). Brecciated ores is widespread in the deposit and consists of subangular fragments of dolomitic limestone and calcareous slate in a matrix of sphalerite-dolomite-quartz assemblage (Fig. 3c). Locally, dissolution breccia is characterized by sphalerite replacing and filling open-spaces within the dolomitic limestone (Fig. 3d). Sphalerite and galena mainly occur as veins and fracture fillings in dolomitic limestone and slate, forming sulfide veins and chaotic sulfide textures (Fig. 3e–g). Massive to semi-massive ore is associated with veins and breccias. It is composed of 60–85% sphalerite with minor dolomite, carbonate, quartz, and remnants of dolomitic host

rock (Fig. 3h).

The sulfide ores are characterized by a relatively uniform mineral assemblage that does not vary substantially with ore types and spatial position in the deposit. Sphalerite, galena, and pyrite are the dominant sulfide minerals, with a generally greater abundance of sphalerite than galena (5:1). Minor amounts of pyrrhotite and chalcocopyrite are present. Dolomite, ankerite, quartz, calcite with minor barite and siderite are the dominant alteration minerals and gangue minerals in the deposit. Other alteration minerals include chlorite, sericite, biotite, talc, apatite, (Ba, K) feldspars and Al-bearing clay minerals. In addition to the dominant sulfide ores, small volumes of oxidized ores occur in the shallower part of the deposit and are composed of anglesite, cerussite, smithsonite, hydrozincite, and jarosite (Zhu et al., 2015).

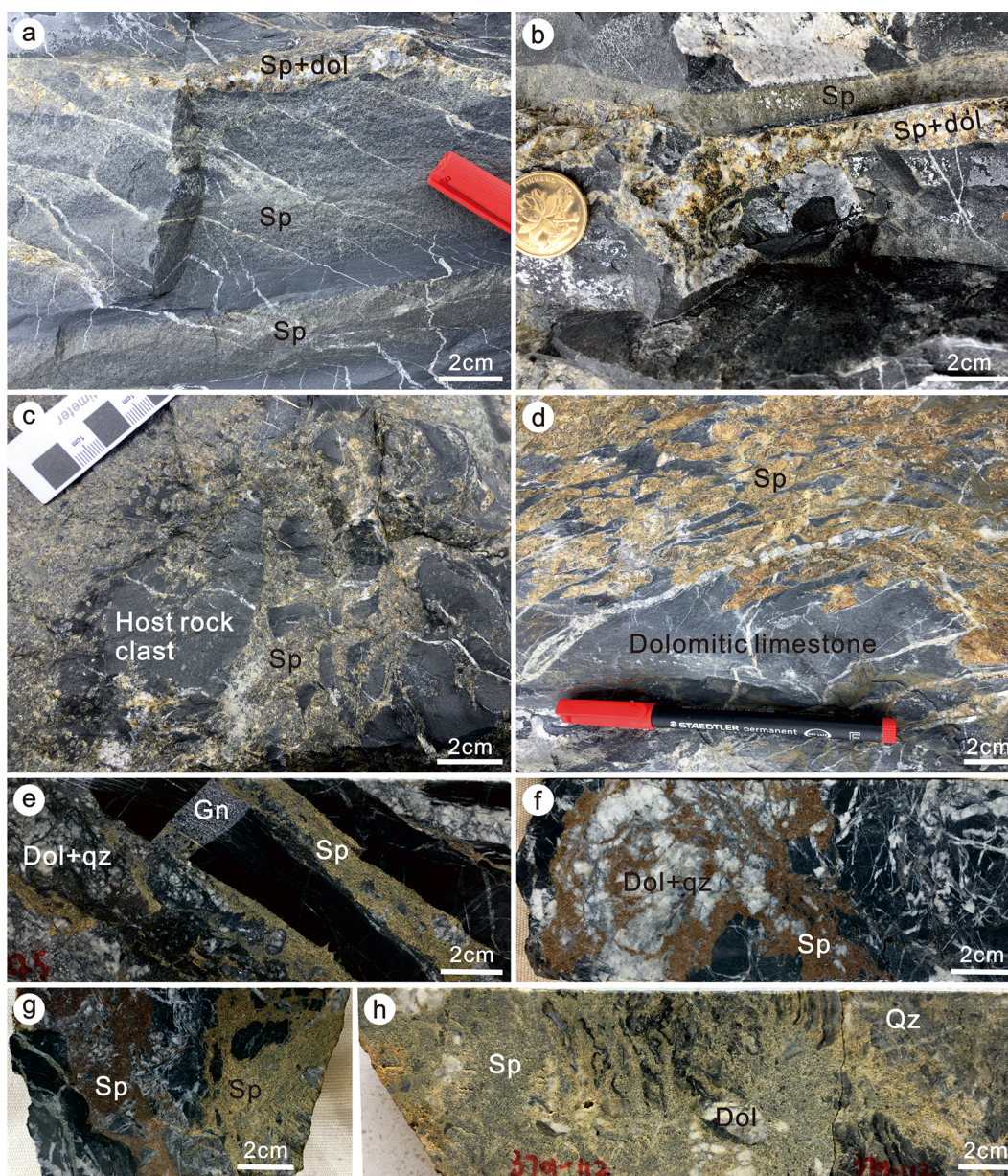


**Fig. 3.** Textural variations of different ore types from the Haerdaban deposit. (a) Fine-grained, disseminated sphalerite crosscut by dolomite veinlet, followed by coarse-grained sphalerite-dolomite veins. (b) Fine-grained, disseminated sphalerite overgrown by coarse-grained sphalerite-dolomite vein. (c) Fragments of dolomitic host rock in a sphalerite matrix (sample H3104). (d) Dissolution sphalerite breccia in the host dolomitic limestone. Note the embayed and corroded contact between the host rock and sphalerite. (e) Sphalerite and galena occurring as veins and fracture fillings in dolomitic limestone (sample 3701-28). (f) Brown sphalerite in dolomitic limestone. (g) Sphalerite in dolomitic limestone with colors varying from dark brown to light yellow (sample 3701-27). (h) Massive sphalerite ore with remnants of dolomitic limestone (sample 3701-112). Abbreviations: Sp = sphalerite, Gn = galena, Dol = dolomite, Qz = quartz.



#### 4. Samples and analytical methods

A suite of 21 core samples for the textural and geochemical study were mainly collected from two drill cores, ZK3701 and ZK4101, which traverse the main orebodies of Zone I (Fig. 2a). One pyrite-rich shale sample was collected from drill core ZK4301. An additional four surface samples of massive ore were collected from the outcrop. The locations of these diamond drill holes and surface samples are shown in Fig. 2 and the depths from which samples came in each of the holes are included in Table 2, along with descriptions of the samples.

##### 4.1. Electron microprobe analyses

Major element analyses of sulfide were completed using a JEOL JXA-8230 electron microprobe at the Institute of Mineral Resources, Chinese Academy of Geological Sciences, Beijing. The analytical conditions involved an acceleration voltage of 15 kV, a beam current of 20 nA, and a defocused electron beam diameter of 5  $\mu\text{m}$ . Natural and synthetic minerals were used as calibration standards. Data reduction was

**Table 2**  
Sample localities and descriptions.

Sample no.	Drill hole/ location	Depth (meters)	Description
3701-6	ZK3701	6	Dark brown, massive sphalerite ore
3701-25		25	Dark brown sphalerite veins and pyrite nodules in host rock
3701-27		27.4	Sphalerite with colors varying from dark brown to yellow
3701-28		28	Occurrence of sphalerite and galena as veins and fracture fillings in dolomitic limestone
3701-30		30	Dolomite-calcite veins with disseminated pyrite
3701-64		64	Brown, massive sphalerite and pyrite veins in dolomitic limestone
3701-90		90.5	Pale yellow, massive sphalerite ore
3701-96		96	Brown, massive sphalerite and pyrite veins in dolomitic limestone
3701-97		97.4	Pale yellow, massive sphalerite ore
3701-112		112.1	Pale yellow, massive sphalerite ore
4101-16	ZK4101	16.8	Dark brown sphalerite vein in host rock
4101-54		54.2	Pyrite-dolomite vein in dolomitic limestone
4101-74		74	Clasts of dolomitic limestone in a matrix of sphalerite-dolomite
4101-100		100.3	Dark brown sphalerite in association with dolomite filling the fracture of host rock
4101-103		103.5	Dark brown sphalerite in association with dolomite filling the fracture of host rock
4101-104		104.2	Disseminated sphalerite in a matrix of dolomite-calcite
4101-105		105	Yellow sphalerite in association with dolomite filling the fracture of host rock
4101-120		120.6	Dark brown, massive sphalerite ore
4101-133		133.4	Dark brown sphalerite vein in host rock
4101-151		151.7	Pyrite aggregates in host rock
4101-152	152.5	Pyrite-dolomite veins in host rock	
4301-176	ZK4301	176.5	Pyrite aggregates in host rock
H3102	Surface sample		Pale yellow, massive sphalerite ore
H3103	Surface sample		Pale yellow, massive sphalerite ore
H3104	Surface sample		Pale yellow, massive sphalerite ore
H840	Surface sample		Pale yellow, massive sphalerite-galena ore

performed using the ZAF correction of JEOL.

##### 4.2. LA-ICP-MS trace element analyses

In situ trace element analyses of pyrite and sphalerite and semi-quantitative mapping of pyrite were completed using LA-ICP-MS at the State Key Laboratory of Ore Deposit Geochemistry, IGCAS, Guiyang. The equipment comprises an Excimer 193 nm RESOLUTION-S155 laser equipped with a double volume sample cell (Laurin Technic S-155) and connected to an Agilent 7700x ICP-MS. Spot analysis was performed using 26- $\mu\text{m}$  beam size at a frequency of 5 Hz with a fluence of 3 J/cm<sup>2</sup>. Semiquantitative mapping was carried out by ablating a series of lines on pyrite grain, using a beam size of 10  $\mu\text{m}$ , a laser frequency of 15 Hz, and a stage speed of 7.5  $\mu\text{m/s}$ . High-purity He (350 mL/min) was applied as a carrier gas. The ablated aerosol was mixed with Ar (900 mL/min) as transport gas before entering the ICP-MS. Each analysis incorporated a background acquisition of approximately 30 s (gas blank) followed by 60 s of data acquisition from the sample.

Reference materials used during analysis were STDGL3 (Danyushvsky et al., 2011) for quantifying chalcophile and siderophile elements, GSE-1G and GSD-1G (Jochum et al., 2005) for quantifying lithophile elements, and pure pyrite (Py) crystal for quantifying sulfur. MASS-1 (USGS) was used as quality control reference material. Spot analyses data were reduced using the LADR software, and trace element maps were processed using Iolite (Paton et al., 2011).

##### 4.3. LA-MC-ICP-MS sulfur isotope analyses

Sulfur isotope compositions of pyrite, sphalerite, and galena were measured in situ using LA-MC-ICP-MS at the State Key Laboratory of Continental Dynamics, Northwest University, Xi'an. The equipment comprises an Excimer 193 nm RESOLUTION M-50 laser ablation system equipped with a double volume sample cell (Laurin Technic S-155) and coupled with a Nu Plasma 1700 MC-ICP-MS (Nu Instruments, UK). Instrumental conditions and analytical procedures are detailed in Chen et al. (2017), Bao et al. (2017) and Yuan et al. (2018). The instrument was operated in high resolution mode. Laser ablation was performed using 30- $\mu\text{m}$  beam size at a frequency of 2 to 3 Hz with a fluence of 3.7 J/cm<sup>2</sup>. High-purity He (280 mL/min) was used as carrier gas and mixed with Ar (960 mL/min) as makeup gas before entering the MC-ICP-MS. The measurements were performed in time-resolved mode, with an integration time of 0.2 s. Each analysis consisted of 30 s background acquisition followed by 50 s data acquisition from sample and 70 s for cleaning the sample cell and plumbing lines.

Instrument drift and mass bias were corrected using a standard-sample bracketing approach with repeated measurements of the standard, before and after each sample. Matrix-matched standards used for calibration were Py-4 (natural pyrite), NBS123 (natural sphalerite), and CBI-3 (natural galena). Sulfur isotope values ( $\delta^{34}\text{S}$ ) are presented in the standard per mil notation (‰) relative to Vienna Canon Diablo Troilite (V-CDT).

## 5. Results

### 5.1. Sulfide mineralogy

Pyrite is ubiquitous in the Haerdaban deposit, occurring in large quantities from the host rocks to massive sulfide ores. It can be grouped into four types on the basis of mineralogical and textural variation (Fig. 4). Porous pyrite (Py1) is identified by its presence in the core of pyrite grain, and a porous texture with abundant inclusions (Fig. 4a, b). Pyrite overgrowth (Py2) on earlier pyrite core is often inclusion poor and share irregular boundary with the core. Euhedral pyrite (Py3) is found mainly in the hydrothermal veins, associated with dolomite, calcite, and quartz (Fig. 4c). It is idiomorphic, coarse grained, inclusion poor, and sometimes contains relict porous pyrite. Pyrite (Py4)

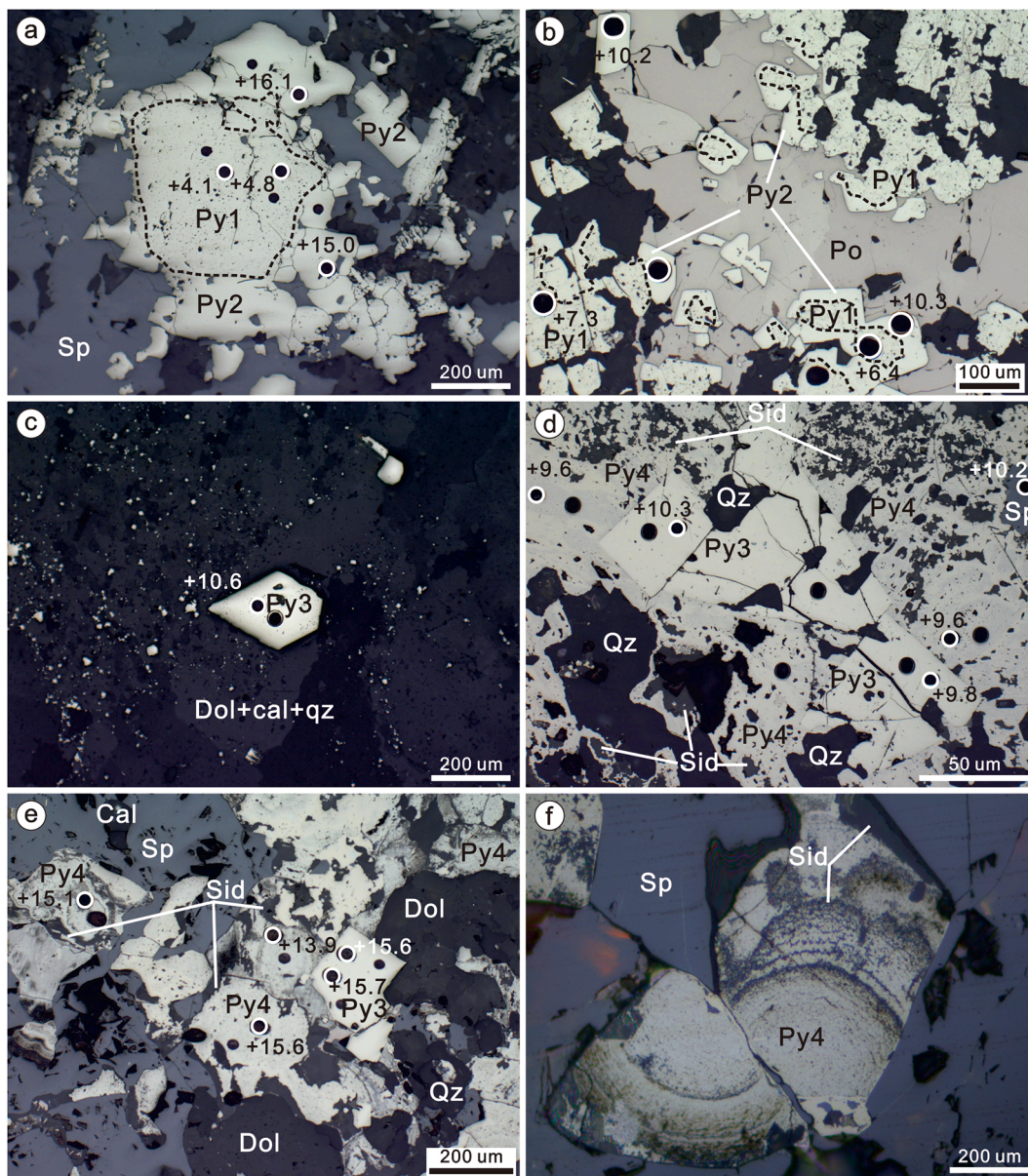


**Fig. 4.** Representative photomicrographs of different pyrite types from the Haerdaban deposit. (a) Porous pyrite (Py1) with inclusion-poor rim (Py2) replaced by sphalerite (sample 3701-27). (b) Porous pyrite (Py1) with inclusion-poor rim (Py2) surrounded by pyrrhotite (sample 4101-151). (c) Coarse-grained euhedral pyrite (Py3) and fine-grained disseminated pyrite in a dolomite-calcite matrix (sample 3701-30). (d) Euhedral pyrite (Py3) surrounded by inclusion-rich anhedral pyrite (Py4); both pyrite types were partly dissolved (sample 3701-25). (e) Euhedral pyrite (Py3) and inclusion-rich anhedral pyrite (Py4), enveloped by sphalerite (sample 3701-6). (f) Fragments of pyrite containing siderite laminae within sphalerite (sample 3701-6). Laser ablation craters with  $\delta^{34}\text{S}$  values (‰) are also shown. Abbreviations: Sp = sphalerite, Py = Pyrite, Po = pyrrhotite, Sid = siderite, Dol = dolomite, Cal = calcite, Qz = quartz.

associated with sphalerite in main-stage ores is characterized by an overall spongy, anhedral appearance, texturally similar to the porous pyrite (Fig. 4d, e). Py4 also comprises concentric pyrite with laminae of siderite, occurring as irregular fragments (Fig. 4f).

Sphalerite is the dominant ore mineral and displays a wide variety of colors, including pale yellow, yellow–brown, and brown to dark brown (Fig. 5). Dark brown sphalerite commonly occurs in narrow veinlets and cracks (Fig. 5a,b) that appears to be a relatively early formation of sphalerite during the main ore-forming event. Light-colored sphalerite typically forms massive, coarse-grained subhedral to anhedral crystal with inclusions of dolomite, quartz, carbonate, talc and sulfides such as pyrite and galena (Fig. 5c). Colloidal (i.e., concentric or colloform) growth, which is a common feature in sphalerite from low temperature (<100 °C) depositional environments (e.g., Barrie et al., 2009) was not observed at Haerdaban.

Galena is volumetrically minor at Haerdaban. It appears to be a late phase in many ore samples and occurs mainly as open space fillings enveloping previous mineral phases such as sphalerite, pyrite and other minerals (Fig. 5c). However, inclusions of galena within sphalerite can also be observed in some samples and represents an earlier generation or a contemporaneous crystallization with sphalerite (Fig. 5d).

A paragenetic sequence for the Haerdaban deposit was developed from field observations and microscope petrographic studies (Fig. 6). The sedimentary to diagenetic stage is represented by precipitation of fine-grained, porous pyrite (Py1) and disseminated sphalerite with fine-grained dolomite, quartz, calcite, apatite and barite in dolomitic limestone and calcareous slate. Mineralization in this stage is volumetrically minor. The hydrothermal stage is the main stage of ore formation. Pyrite overgrowth (Py2) and euhedral pyrite (Py3) are precipitated in this stage and occurred slightly earlier than sphalerite and galena as



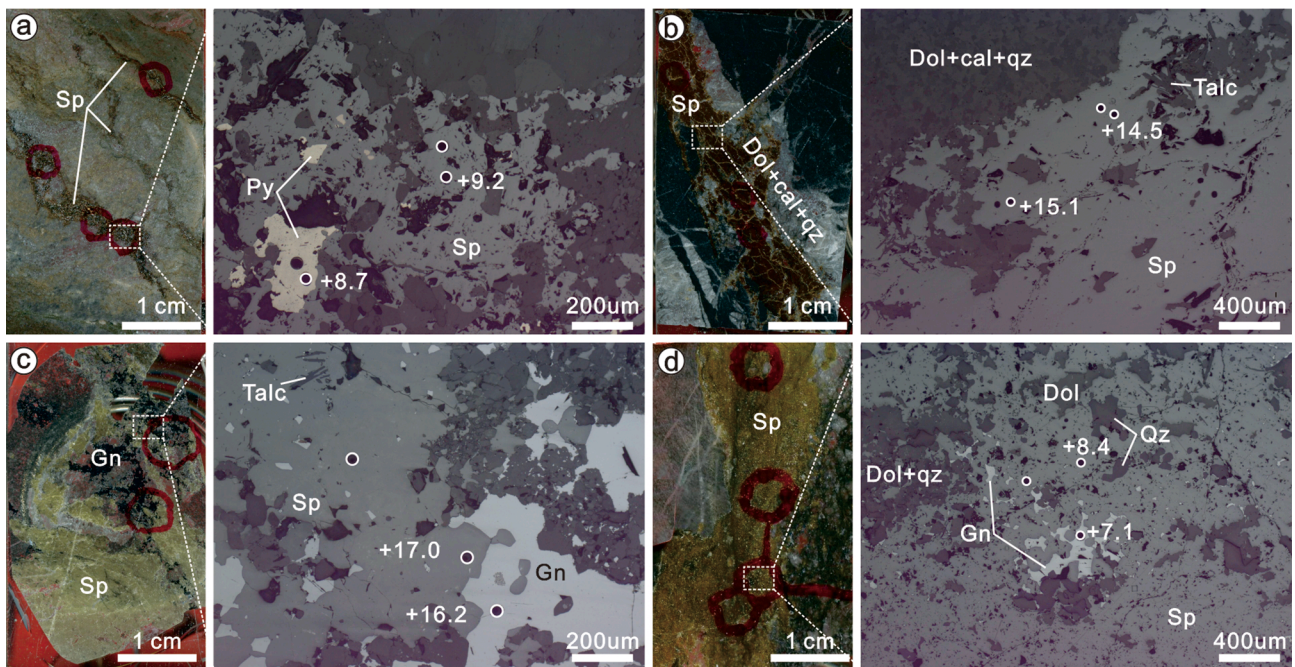


Fig. 5. Images of thin sections and corresponding photomicrographs for sphalerite of varying color at Haerdaban. (a) Dark brown sphalerite vein (sample 4101-133). (b) Dark brown sphalerite in association with dolomite along the fracture of host rock (sample 4101-100). (c) Pale yellow sphalerite associated with galena (sample H840). (d) Brown sphalerite with galena inclusions (sample 3701-28). Laser ablation craters with  $\delta^{34}\text{S}$  values (‰) are also shown. Abbreviations: Sp = sphalerite, Gn = galena, Py = Pyrite, Dol = dolomite, Cal = calcite, Qz = quartz.

	Sedimentation/ diagenesis	Main mineralization Hydrothermal	Supergene
Pyrite	—————	—————	
Pyrrhotite		—————	
Sphalerite	—————	—————	
Galena	-----	—————	
Dolomite	—————	—————	
Calcite	—————	—————	
Siderite		—————	
Quartz	—————	—————	
Barite	—————		
Chlorite		—————	
Sericite		—————	
Apatite	-----	-----	
Smithsonite			-----
Cerussite			-----
Anglesite			-----

main    
  minor    
  locally occurring

Fig. 6. Generalized paragenetic sequence of minerals in the Haerdaban Zn-Pb deposit.



demonstrated by corrosion of some pyrite. Trace pyrrhotite was considered to form through metamorphism of pyrite. Sphalerite was the most significant sulfide in ores that precipitated in this stage in this stage. Spongy pyrite (Py4) was precipitated synchronously with sphalerite. Minor galena was precipitated later within in veins and vugs. The dominant gangue mineral associated with main-stage ores is hydrothermal dolomite and quartz; siderite, calcite, chlorite, sericite, talc, apatite, (Ba, K) feldspars are volumetrically minor. Small volumes of sulfide ore in the shallower part were affected by supergene stage, which are characterized by anglesite, cerussite, smithsonite, hydrozincite, and jarosite.

## 5.2. Trace elements in pyrite and sphalerite

### 5.2.1. Pyrite

The trace element compositions of pyrite obtained by LA-ICP-MS analysis are summarized in Table 3 and plotted in Fig. 7. The complete data can be found in the Supplementary Table 1. Pyrite in the Haerdaban contains a diverse suite of trace elements, including Mn, Co, Ni, Cu, Zn, As, Se, Mo, Ag, Sb, Tl, Pb, and Bi. The contents of these elements show a wide variability among different pyrite types, with some elements varying over several orders of magnitude. The LA-ICP-MS spot analyses and imaging reveal that the trace element variability is coincident with textural variability in different pyrite types (Fig. 8).

The compositions of porous pyrite core (Py1) are variable but are generally enriched in Mn (0.46–758.02 ppm), Co (0.1–283.91 ppm), Ni (0.48–300.35 ppm), Cu (8.33–818.69 ppm), Zn (1.18–408.86 ppm), As (40.2–641.57 ppm), Se (2.19–7.27 ppm), Ag (0.85–3.37 ppm), Sn (0.12–58.72 ppm), Sb (3.9–80.45 ppm), Ba (0.06–81.51 ppm), Tl (0.04–188.86 ppm), Pb (47.33–1139.3 ppm), and Bi (0.06–24.24 ppm), in comparison with the later generations (Table 3; Fig. 7). The pyrite overgrowth (Py2) is depleted in most trace elements except Co and Ni, which exhibit a slight enrichment (up to 1014.37 ppm and 580.26 ppm, respectively), when compared with the porous core. The marked chemical contrast between pyrite core and overgrowth is clearly displayed in the LA-ICP-MS element imaging (Fig. 8). Similar to the pyrite overgrowth, the euhedral pyrite (Py3) is also enriched in As (134.92–4855.27 ppm), Ni (5.1–188.71 ppm), and Co (7.52–9491.96 ppm), but depleted in any other trace elements. Although pyrite (Py4) in main-stage ore is characterized by high density of mineral inclusions and a spongy appearance, it is depleted in most trace elements, except Ni (24.58–1344.95 ppm) and Sb (13.05–777.50 ppm), relative to the porous pyrite (Table 3; Fig. 7). In particular, the very low concentration of As from below detection limit (BDL) to 24.4 ppm in Py4 stands in contrast to the other pyrite types, which contain approximately >40.2 ppm As (up to 4855.27 ppm). Trace element LA-ICP-MS images (Fig. 8) revealed that the hydrothermal overprint produces enrichments of Sb, Pb, Ba and to a lesser extent of Mn, Ag, Tl, and Cu on the margin of euhedral pyrite (Py3), whereas Co, Ni, As were retained in the pyrite lattice.

### 5.2.2. Sphalerite

A total of 173 analyses were obtained from sphalerite of different color types in 21 samples. The results are summarized in Table 4 and plotted in Fig. 9. The complete data are presented in the Supplementary Table 2. The fairly flat pattern for the counts of elements listed (Mn, Fe, Co, Ga, Cd, and In) and their similar pattern to the Zn counts (not shown) suggest that these elements are mainly contained within the sphalerite lattice.

Sphalerite of different color types exhibit a great variation in minor and trace element contents (Fig. 9). In particular, a distinct trend of decreasing Fe contents can be observed from early dark brown (4.95 to 6.12 wt%) through brown sphalerite (1.73 to 3.26 wt%) and yellow-brown sphalerite (0.99 to 1.57 wt%) to pale yellow sphalerite (0.25 to 1.1 wt%). Cadmium is the second abundant trace element in sphalerite, with contents varying from 524 to 1875 ppm. There is no clear

correlation between Cd content and color variation, although the dark brown sphalerite seems to have slightly high Cd contents (923 to 1875 ppm). The Mn contents range from 47 to 407 ppm and show slight variation among the sphalerite types, with lower Mn contents (47 to 378 ppm; average 120 ppm) tend to be found in light-colored sphalerite.

The majority of Co contents range from BDL to 32.93 ppm, but content of up to 155.98 ppm is recorded in sphalerite from narrow veinlet (sample 4101-133). Co contents show a moderate correlation with color, with average Co content in dark-colored sphalerite is higher than the light-colored ones (91.93 ppm versus 0.86 ppm). The Ga contents are variable, but the average content in dark brown sphalerite is slightly lower (0.55–13.47 ppm; average 3.44 ppm) than that of all other sphalerite types (1.1–50.88 ppm; average 12.8 ppm). The Ge contents in all sphalerite types are generally below 3.2 ppm, and are not detected in every sample. The In contents is dominantly below 1.92 ppm, except for two dark brown sphalerite (samples 4101-133, 3701-25), in which elevated values of 2.42–9.89 ppm and 5.39–5.60 ppm are recorded. Sn in sphalerite is mostly below 4.58 ppm for all types, with some individual analyses yielding values as high 10.23 ppm.

Contents of Ag, Sb, Cu and Pb are similarly variable in all sphalerite types. The contents of Ag and Sb are generally less than 15 ppm, although elevated values of 39.35 ppm are observed for Sb. Anomalous high values of Cu (up to 80.06 ppm) and Pb (up to 130.78 ppm) characterize all sphalerite types (Table 4; Fig. 9), probably related to the presence of submicroscopic inclusions of chalcopyrite and galena (as observed in laser ablation profiles), respectively. The contents of other elements, such as As and Tl, which have been found in sphalerite, are mostly below detection limits in all measured sphalerite.

## 5.3. Sulfur isotopes

The results of in situ sulfur isotope analyses on pyrite, sphalerite and galena from the Haerdaban deposit are summarized in Table 5 and plotted in Fig. 10. The complete data can be found in the Supplementary Table 3. Selected data points within their textural context are shown in Figs. 4, 5. In general, all sulfide minerals exhibit consistently positive  $\delta^{34}\text{S}$  values, but considerable isotopic variability occurs in different sulfide types.

There is a large spread in  $\delta^{34}\text{S}$  values for the pyrite core and overgrowth. Porous pyrite cores (Py1) have uniform  $\delta^{34}\text{S}$  values between +3.9 and +8.8‰ (n = 27; Fig. 10a). In contrast, the  $\delta^{34}\text{S}$  values of the pyrite rims (Py2) range from +7.5 to +16.8‰ (n = 32; Fig. 10a), which are 2.0 to 12.2 ‰ heavier than the porous cores. The  $\delta^{34}\text{S}$  values of the euhedral pyrite (Py3) vary from +9.8 to +16.0‰ (n = 14; Fig. 10a). Inclusion-rich pyrites (Py4) associated with sphalerite show a range of  $\delta^{34}\text{S}$  values between +8.1 and +15.6‰ (n = 18; Fig. 10a).

Sphalerite sulfur isotope data exhibit two dominant populations with vein sphalerite have lower  $\delta^{34}\text{S}$  values (+8.4 to +13.0‰, n = 30; Fig. 10b), whereas massive sphalerite have heavier  $\delta^{34}\text{S}$  values (+13.8 to +18.3‰, n = 81; Fig. 10b). The highest values of +18.3‰ correspond to the pale-yellow massive sphalerite. Sulfur in galena is isotopically lighter than that of associated sphalerite and also displays a bimodal distribution in  $\delta^{34}\text{S}$  values. Galena associated with dark-colored sphalerite has  $\delta^{34}\text{S}$  values between +7.0 and +10.3‰ (n = 19; Fig. 10c), whereas galena contemporaneous with light-colored sphalerite show  $\delta^{34}\text{S}$  values between +16.2 and +16.7‰ (n = 5; Fig. 10c).

## 6. Discussion

### 6.1. Pyrite texture and chemical variations

The incorporation of trace elements in pyrite, either by substitution within crystal lattice or as nanoparticles or micro-inclusions, is thought to reflect the composition of hydrothermal fluids and the varying conditions in which pyrite formed (Huston et al., 1995; Deditius et al., 2011; Maslennikov et al., 2009; Genna and Gaboury 2015; Wohlgenuth-

Table 3

Summary of LA-ICP-MS trace element data (ppm) for pyrite from the Haerdaban deposit.

			Mn	Co	Ni	Cu	Zn	As	Se	Ag	Sn	Sb	Ba	Tl	Pb	Bi	Co/Ni	
Sample	Description	Avg. DL	0.47	0.06	0.44	0.31	1.31	0.29	2.3	0.53	0.1	0.2	0.03	0.04	0.06	0.03		
3701-6	Euhedral	Mean(7)	–	20.18	6.78	1.08	24.06	568.73	–	–	–	0.51	0.06	–	1.06	–	3.07	
		SD	–	9.73	1.93	–	–	290.87	–	–	–	0.31	0.04	–	1.01	–	1.46	
		Min	–	7.52	5.10	1.08	24.06	341.32	–	–	–	0.24	0.03	–	0.28	–	1.04	
		Max	–	32.01	10.61	1.08	24.06	1111.57	–	–	–	0.96	0.11	–	2.54	–	4.73	
	Inclusion-rich, associated with sphalerite	Mean(11)	4.76	–	27.37	0.40	1192.40	8.10	–	–	0.44	179.20	1.97	31.77	1.41	–	–	–
		SD	6.46	–	2.26	0.06	2396.52	8.93	–	–	–	212.48	1.03	58.42	1.57	–	–	–
		Min	0.61	–	24.58	0.36	13.98	1.20	–	–	0.44	13.05	0.80	0.03	0.35	–	–	–
		Max	17.36	–	31.59	0.44	6119.70	24.36	–	–	0.44	777.50	4.35	134.60	5.83	–	–	–
		Euhedral	Mean(5)	1.93	4118.28	56.58	5.47	2.04	1395.77	6.54	0.71	0.22	7.70	16.58	0.11	309.29	0.11	172.46
			SD	–	4225.25	33.55	2.88	0.38	1975.47	1.87	–	–	4.32	23.92	0.08	368.77	0.06	284.15
3701-25	Euhedral	Min	1.93	307.06	14.12	2.84	1.63	134.92	3.66	0.71	0.22	4.07	0.10	0.05	0.84	0.05	2.99	
		Max	1.93	9491.96	102.54	8.77	2.38	4855.27	8.90	0.71	0.22	13.97	58.17	0.17	892.27	0.16	672.45	
		Mean(5)	0.98	9.24	1092.92	0.75	7.89	0.37	11.60	0.94	0.14	59.58	1.86	2.54	341.84	0.08	0.01	
		SD	0.57	18.25	154.35	1.05	3.43	0.13	1.89	0.93	–	32.69	1.34	4.69	307.92	0.06	0.01	
	Inclusion-rich, associated with sphalerite	Min	0.43	1.02	947.56	0.20	2.95	0.20	9.72	0.28	0.14	25.01	0.75	0.07	18.60	0.04	–	
		Max	1.79	41.89	1344.95	2.62	11.99	0.48	14.67	1.60	0.14	113.12	3.87	10.90	853.16	0.12	0.03	
		Porous core	Mean(16)	10.79	0.45	2.13	18.19	62.15	145.39	–	2.20	1.11	16.88	8.48	54.45	275.14	0.09	0.11
			SD	7.22	0.36	2.03	7.67	133.06	105.92	–	0.59	1.43	8.36	9.50	53.29	149.81	0.03	0.06
			Min	0.76	0.10	0.48	8.33	2.58	40.20	–	1.22	0.12	6.76	0.50	3.34	86.39	0.06	–
			Max	30.37	1.00	6.12	35.92	408.86	415.14	–	3.37	4.68	31.87	34.93	188.86	658.28	0.12	0.22
Overgrowth	Mean(14)	2.24	2.45	9.99	1.14	159.63	150.54	–	0.25	–	1.41	1.49	0.27	17.23	–	0.30		
	SD	0.37	2.85	11.81	0.71	317.97	64.49	–	0.14	–	1.13	3.07	0.33	18.62	–	0.21		
	Min	1.97	0.34	1.65	0.42	3.16	67.20	–	0.15	–	0.27	0.03	0.06	0.94	–	0.08		
	Max	2.50	10.72	44.30	2.39	801.77	276.22	–	0.35	–	3.42	9.05	0.92	58.37	–	0.85		
3701-30	Euhedral	Mean(5)	0.75	113.58	105.80	5.96	1.80	763.28	–	–	–	5.05	0.08	0.22	19.00	0.06	1.15	
		SD	–	83.46	65.34	0.38	0.27	465.13	–	–	–	–	–	–	26.65	–	0.52	
		Min	0.75	38.18	27.27	5.69	1.61	183.38	–	–	–	5.05	0.08	0.22	0.15	0.06	0.62	
		Max	0.75	243.43	188.71	6.23	1.99	1315.34	–	–	–	5.05	0.08	0.22	37.84	0.06	1.88	
3701-64	Overgrowth	Mean(6)	–	9.49	12.70	8.30	2.34	211.18	–	–	–	0.42	0.95	–	1.72	–	0.84	
		SD	–	4.08	6.09	–	1.34	71.41	–	–	–	0.15	1.46	–	2.68	–	0.49	
		Min	–	4.43	9.17	8.30	1.43	103.65	–	–	–	0.31	0.06	–	0.13	–	0.42	
		Max	–	15.66	24.98	8.30	4.32	303.82	–	–	–	0.52	2.64	–	6.94	–	1.68	
4101-54	Porous core	Mean(4)	14.66	0.27	1.70	20.17	3.83	176.56	2.40	1.71	0.37	30.32	0.37	20.46	466.49	0.39	0.08	
		SD	13.74	0.18	0.64	6.87	3.22	55.23	0.29	0.94	0.05	12.72	0.32	24.14	462.52	0.11	0.08	
		Min	2.62	0.14	0.76	11.38	1.33	121.00	2.19	0.85	0.31	17.17	0.06	6.16	90.71	0.27	–	
		Max	31.70	0.39	2.19	26.39	7.46	251.93	2.60	2.97	0.42	46.91	0.77	56.50	1139.30	0.53	0.20	
	Overgrowth	Mean(4)	–	0.69	7.05	0.70	–	476.93	3.53	–	–	0.86	0.05	–	3.93	–	0.12	
		SD	–	0.71	8.38	0.27	–	60.49	0.75	–	–	0.95	–	–	3.75	–	0.05	
		Min	–	0.19	2.13	0.51	–	402.45	2.69	–	–	0.26	0.05	–	0.95	–	0.09	
		Max	–	1.73	19.57	0.89	–	545.86	4.30	–	–	1.95	0.05	–	8.14	–	0.19	
4101-151	Porous core	Mean(3)	583.45	148.00	101.89	88.82	112.35	183.73	4.41	1.40	13.62	54.95	16.26	4.19	708.70	14.90	1.52	
		SD	200.75	50.22	42.23	29.35	40.92	50.82	1.27	0.34	5.92	10.02	4.02	0.49	276.53	8.09	0.42	
		Min	364.09	92.88	61.52	67.46	67.89	125.12	3.51	1.01	8.98	46.25	12.01	3.80	390.34	10.04	1.10	
		Max	758.02	191.15	145.77	122.29	148.42	215.68	5.31	1.62	20.28	65.90	20.00	4.74	889.22	24.24	1.94	
	Overgrowth	Mean(3)	2.97	466.73	154.26	1.75	2.16	353.34	7.04	0.70	0.16	4.26	7.25	0.81	27.09	0.78	4.27	
		SD	–	477.41	113.22	1.85	–	275.45	2.56	–	0.01	4.70	10.11	0.91	27.36	0.74	3.48	
		Min	2.97	138.23	50.12	0.44	2.16	153.19	5.51	0.70	0.15	0.38	0.10	0.17	1.38	0.05	0.50	
		Max	2.97	1014.37	274.77	3.06	2.16	667.49	9.99	0.70	0.16	9.49	14.40	1.45	55.85	1.53	7.36	
4101-152	Overgrowth	Mean(6)	–	99.87	225.88	4.82	–	550.09	9.63	–	0.10	1.62	0.12	–	4.14	0.58	0.63	
		SD	–	113.19	187.53	5.35	–	173.52	6.58	–	–	1.63	–	–	4.80	0.88	0.61	
		Min	–	15.31	88.13	1.03	–	420.04	3.15	–	0.10	0.18	0.12	–	0.10	0.04	0.04	
		Max	–	313.16	580.26	8.60	–	884.18	20.55	–	0.10	3.39	0.12	–	10.12	1.60	1.53	
4301-176	Porous core	Mean(10)	160.65	119.98	165.11	130.51	26.27	413.80	5.26	2.19	11.63	32.39	30.01	9.30	396.13	4.72	0.68	
		SD	187.23	86.85	86.08	247.90	32.10	127.68	1.58	0.79	17.76	24.86	25.94	12.51	282.24	2.99	0.31	
		Min	0.46	6.95	17.75	10.04	1.18	221.28	2.71	0.90	0.33	3.90	7.02	0.04	47.33	0.54	0.39	
		Max	503.31	283.91	300.35	818.69	74.56	641.57	7.27	3.09	58.72	80.45	81.51	35.72	785.52	9.09	1.33	
	Overgrowth	Mean(3)	–	217.95	205.57	0.58	0.95	494.33	6.96	–	–	1.16	0.03	0.05	1.56	0.17	1.00	
		SD	–	188.61	95.24	–	0.10	338.91	0.11	–	–	–	0.01	–	1.20	0.23	0.94	
		Min	–	1.33	139.71	0.58	0.84	106.02	6.84	–	–	1.16	0.02	0.05	0.60	0.04	0.01	
		Max	–	345.82	314.77	0.58	1.03	730.61	7.05	–	–	1.16	0.04	0.05	2.90	0.43	1.89	

Note: Avg. DL = average detection limit; SD = standard deviation; Number in bracket refers to the number of analyses.

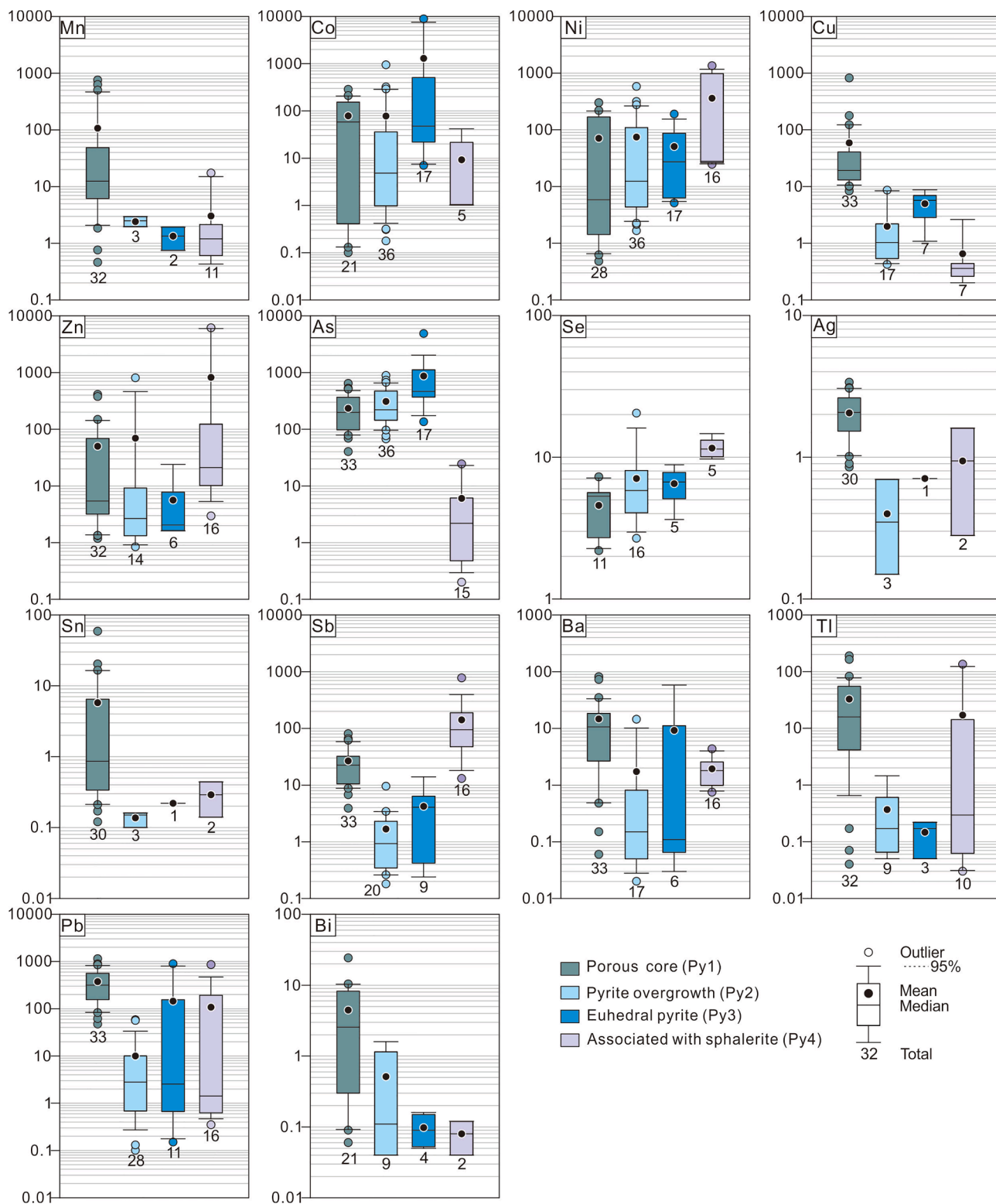


Fig. 7. Box and whisker plots illustrating the trace element variation in different pyrite types from the Haerdaban deposit.

Ueberwasser et al., 2015; Keith et al., 2016). As a ubiquitous sulfide phase in all mineralization stages at Haerdaban, pyrite with varied textures and trace element compositions could provide a better record of the signature of the ore-forming fluid and its evolution.

Petrographic observations indicate that pyrite at Haerdaban usually have inclusion-rich cores with irregular outlines surrounded by inclusion-free rims (Fig. 4). The porous pyrite core, considered as the

earliest generation of pyrite, is texturally identical to syngenetic or diagenetic pyrite that is common in sediment-hosted deposits (e.g.,). In most cases, the porous texture and abundance of inclusions indicated rapid nucleation of pyrite from supersaturated solution at low temperatures (Large et al., 2009). The porous pyrite core is geochemically distinguished from all later pyrite generations by enrichment in Mn, Ag, Sb, Tl, Ba, Pb, Cu, and Zn (Table 3, Figs. 7, 8), consistent with chemical



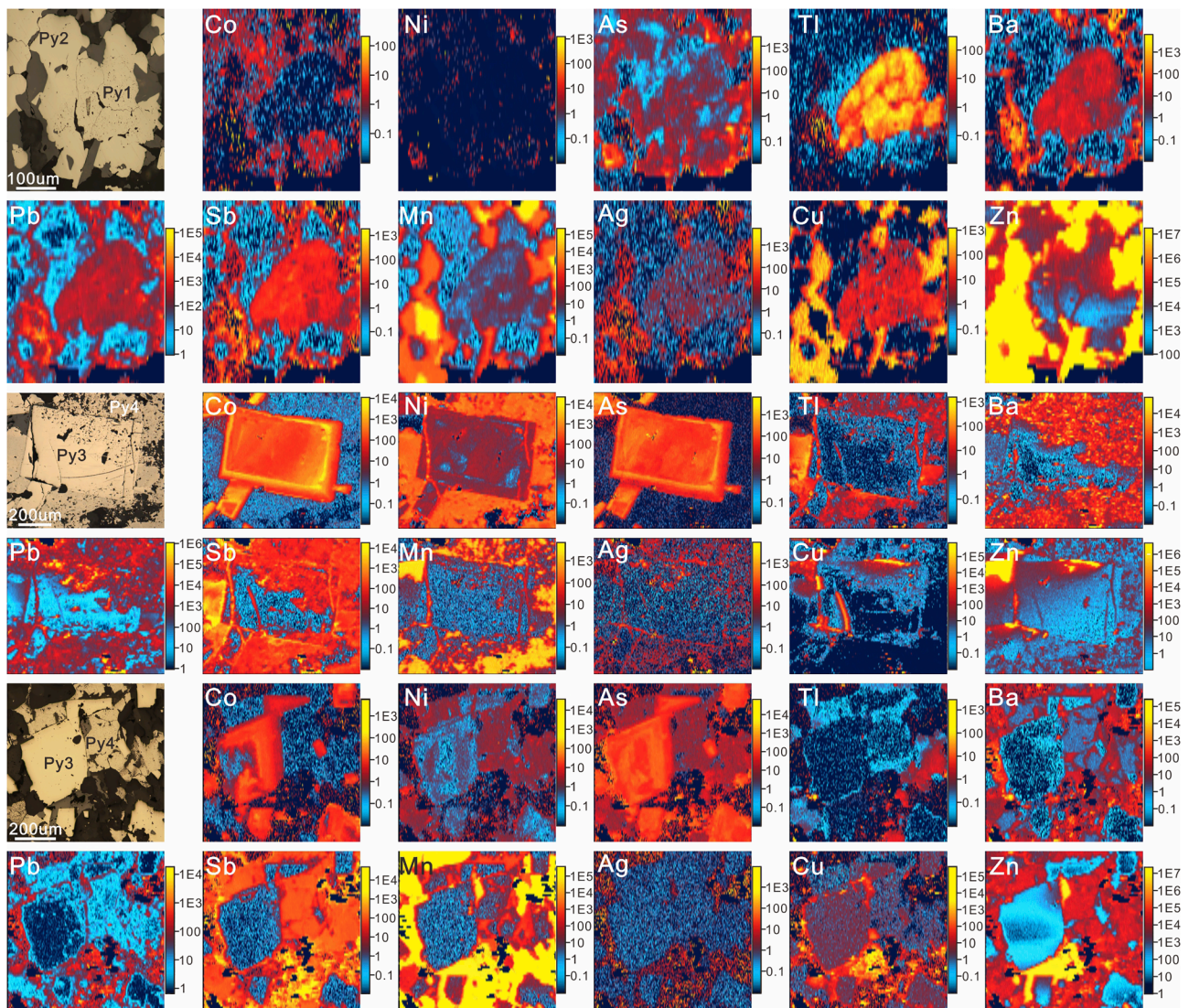


**Fig. 8.** Reflected light photomicrographs and LA-ICP-MS trace element images of different pyrite types from the Haerdaban deposit. Semiquantitative concentrations are presented in false-color logarithmic scale. (a) The porous core (Py1) is identified by enrichment in Sb, Tl, Ba, Pb, Cu, Mn, and Ag, whereas the inclusion-poor rim (Py2) is enriched in Co but lower in all other trace elements (sample 3701-27). (b) The euhedral pyrite (Py3) shows enrichment in Co and As, but depleted in all other trace elements, compared with the surrounding Py4. Note that hydrothermal overprint produced enrichments of Sb, Pb, Ba and to a lesser extent of Mn, Ag, Tl, and Cu on the margin of cubic pyrite, whereas Co, Ni, As were retained in the pyrite lattice (sample 3701-25). (c) The euhedral pyrite (Py3) is enriched in Co and As, whereas the surrounding Py4 shows enrichment in Ni, Sb, and Zn (sample 3701-6).

signature of sedimentary to diagenetic pyrite found in sub-oxic to anoxic environments (e.g., Large et al., 2007, 2009; Ulrich et al., 2011). In these environments, the large quantity of trace elements in porous pyrite is likely due to the rapid crystallization and large surface to volume ratio, which facilitated the incorporation of elements into pyrite as inclusions or by adsorption (Large et al., 2009; Steadman et al., 2021). The elemental association of Mn, Ag, Sb, Tl, Pb, and Zn (the so-called epithermal suite) that may be added in the water column via hydrothermal exhalations (Mukherjee and Large, 2017), indicate a fluid derived from an evolved continental crust (Leach et al., 2005; Wilkinson, 2014) or in some cases with a magmatic fluid influence (e.g., Hedenquist and Lowenstern, 1994; Sillitoe et al., 1996; Simmons et al., 2016).

The anhedral pyrite overgrowths and euhedral pyrite show marked contrast in texture and trace element pattern relative to the porous pyrite. They are inclusion-free and depleted in most trace elements (Figs. 7, 8), except Co and Ni. The boundaries between the anhedral pyrite overgrowths and porous cores are generally irregular, with some evidence for partial replacement of pyrite cores. The boundary between the core and overgrowth is commonly irregular, suggesting partial

dissolution of Py1 during the growth of Py2. The cubic pyrite is typically coarse-grained and sometimes contains relict porous pyrite. These textures indicate that both pyrite overgrowths and euhedral pyrite have nucleated on, or replaced early porous pyrite. Recrystallization of pyrite has been widely observed in SEDEX deposits (e.g., Red Dog, Howard's Pass; Kelley et al., 2004; Gadd et al., 2016) and VMS deposits (e.g., Herzig and Hannington, 1995) in sea-floor settings, where it was attributed to the upwelling hydrothermal fluids. In this process, porous pyrite tends to expel its inclusions and loosely bound elements (e.g., Mn, Ag, Sb, Cu, Pb, Zn and Ba) to the ambient fluids, forming the inclusion-free and trace element-depleted pyrite (Huston et al., 1995; Large et al., 2007).

Pyrite 4 associated with sphalerite of main-ore stage is characterized by high density of inclusions, texturally similar to the porous pyrite core. The pyrite 4 likely crystallized rapidly from pyrite-supersaturated solutions in a manner analogous to porous pyrite (Butler and Rickard, 2000). It is expected that this pyrite would contain high contents of trace elements, since the rapid growth under non-equilibrium conditions favoring the uptake of elements by pyrite (Keith et al., 2018; Reich et al.,



**Table 4**  
Summary of major (wt%) and trace element data (ppm) for sphalerite from the Haerdaban deposit.

			Zn (%)	Fe (%)	Mn	Co	Ni	Cu	Ga	Ge	Ag	Cd	In	Sn	Sb	Hg	Pb	As	Se	Tl	Zn/Cd	Temperature
Sample	Description	Avg. DL			0.41	0.05	0.40	0.31	0.09	0.70	0.50	0.25	0.01	0.10	0.20	4.13	0.10	0.29	2.06	0.04		
3701-6	Dark brown, massive	Mean (10)	60.20	5.32	138	–	0.35	12.19	1.15	1.73	0.60	1513	0.04	0.60	1.78	84.11	3.29	–	–	–	414	266
		SD	0.59	0.24	20	–	–	8.21	0.16	0.63	0.11	306	0.02	0.23	2.11	11.16	3.82	–	–	–	89	6
		Min	59.17	5.15	103	–	0.35	6.21	0.95	1.00	0.42	1108	0.02	0.33	0.19	58.78	0.43	–	–	–	320	258
		Max	60.76	5.95	159	–	0.35	28.41	1.41	3.20	0.80	1875	0.07	0.97	6.93	99.94	11.71	–	–	–	548	275
3701-25	Dark brown, vein	Mean (4)	59.13	5.68	378	7.31	–	32.40	12.30	1.86	2.08	1216	5.52	0.86	5.59	45.55	50.72	–	9.96	–	486	281
		SD	0.04	0.09	8	0.83	–	7.71	1.22	0.03	0.80	16	0.09	0.44	4.61	1.41	33.68	–	1.64	–	7	2
		Min	59.09	5.60	370	6.29	–	26.97	10.58	1.84	1.40	1195	5.39	0.33	1.76	44.01	18.82	–	8.57	–	480	279
		Max	59.18	5.80	389	7.99	–	43.76	13.47	1.91	3.20	1231	5.60	1.23	12.28	47.41	84.34	–	12.24	–	495	283
3701-27	Brown, massive	Mean (11)	63.99	2.03	112	–	–	20.33	11.97	1.31	1.75	714	0.12	1.98	1.41	44.27	7.89	0.41	2.52	0.08	915	229
		SD	0.32	0.17	17	–	–	1.89	3.17	0.54	0.81	108	0.02	0.86	0.95	7.47	6.27	0.20	0.45	0.04	130	4
		Min	63.58	1.73	73	–	–	17.67	9.09	0.82	0.95	593	0.08	0.51	0.33	32.13	1.16	0.18	1.61	0.05	744	222
	Pale yellow, massive	Max	64.46	2.24	134	–	–	23.65	18.20	2.66	3.20	866	0.15	3.03	3.10	55.78	21.65	0.77	3.05	0.16	1073	234
		Mean (6)	66.30	0.54	125	–	–	20.15	9.38	1.35	2.17	622	0.13	2.12	1.21	46.00	5.12	0.95	3.13	0.06	1065	207
		SD	0.22	0.20	10	–	–	4.19	0.74	0.26	1.20	11	0.04	0.62	1.13	5.39	3.58	0.48	0.60	0.02	18	6
3701-28	Yellow brown, vein	Min	66.01	0.33	112	–	–	15.64	7.98	1.11	0.84	609	0.04	1.03	0.10	38.96	1.28	0.45	2.13	0.04	1039	195
		Max	66.63	0.78	134	–	–	28.01	9.95	1.76	4.29	640	0.16	2.82	3.34	52.49	11.41	1.71	3.59	0.09	1089	214
		Mean (10)	64.42	1.48	133	3.45	1.22	34.78	21.97	1.24	3.38	945	1.05	0.53	11.11	100.04	31.74	0.68	1.80	0.12	682	232
	Brown, massive	SD	0.31	0.05	15	0.33	0.63	6.49	2.04	0.60	3.01	35	0.17	0.36	12.72	4.74	39.61	0.23	0.23	0.06	23	8
		Min	63.94	1.40	112	2.94	0.47	28.57	19.19	0.74	0.59	896	0.84	0.14	0.53	88.40	0.75	0.39	1.39	0.04	642	221
		Max	64.80	1.57	152	4.07	2.59	46.03	24.82	2.23	10.16	1007	1.36	1.30	39.35	104.59	130.78	1.03	2.07	0.18	714	247
3701-64	Brown, massive	Mean (8)	63.59	2.05	383	–	–	12.29	8.51	1.22	0.75	1044	0.10	1.28	0.92	90.40	1.85	0.48	–	–	614	252
		SD	0.23	0.10	21	–	–	2.32	1.79	0.23	0.11	96	0.04	0.88	0.83	3.84	2.55	–	–	–	56	7
		Min	63.22	1.95	340	–	–	8.78	6.04	1.02	0.63	928	0.04	0.31	0.16	84.45	0.22	0.48	–	–	550	242
		Max	64.01	2.21	407	–	–	15.58	10.97	1.51	0.92	1156	0.18	2.59	1.93	95.66	6.40	0.48	–	–	684	260
3701-90	Pale yellow, massive	Mean (8)	65.90	0.69	135	1.09	1.03	24.36	20.49	1.39	1.38	678	0.02	0.49	2.07	58.37	3.26	0.70	–	0.04	972	190
		SD	0.19	0.02	3	0.13	0.19	2.20	1.49	1.01	0.59	9	–	0.42	0.78	2.26	4.57	0.27	–	–	15	11
		Min	65.57	0.67	131	0.93	0.78	22.09	17.70	0.71	0.97	668	0.02	0.10	1.51	55.81	0.21	0.51	–	0.04	954	172
		Max	66.10	0.71	139	1.30	1.33	28.19	22.28	3.12	2.77	691	0.02	0.96	2.62	62.15	12.83	0.88	–	0.04	990	205
3701-96	Pale yellow, massive	Mean (7)	65.29	0.96	350	0.67	1.03	15.69	9.73	1.58	0.67	741	0.21	0.40	0.32	93.04	2.21	0.22	–	–	883	232
		SD	0.20	0.06	29	0.26	0.50	3.34	2.09	0.68	0.25	40	0.07	0.05	0.15	4.58	1.11	0.05	–	–	49	7
		Min	65.03	0.90	297	0.37	0.39	10.84	7.61	0.75	0.42	691	0.13	0.34	0.09	84.20	0.59	0.15	–	–	810	225
		Max	65.53	1.05	378	0.96	1.56	19.79	12.66	2.28	1.02	803	0.33	0.46	0.49	98.52	3.34	0.27	–	–	947	244
3701-97	Pale yellow, massive	Mean (5)	64.84	0.98	89	0.77	1.00	6.51	1.63	1.28	0.60	1037	0.07	0.32	0.43	71.12	1.12	0.43	–	–	625	232
		SD	0.60	0.08	5	0.09	0.30	1.38	0.45	0.28	0.08	19	0.02	0.05	0.34	12.56	1.17	0.15	–	–	14	2
		Min	64.37	0.88	80	0.66	0.71	5.58	1.10	0.86	0.52	1005	0.04	0.27	0.21	58.88	0.42	0.28	–	–	613	230
		Max	65.88	1.10	94	0.85	1.43	8.90	2.25	1.61	0.69	1054	0.09	0.40	1.02	90.22	3.19	0.64	–	–	645	235
3701-112	Pale yellow, massive	Mean (10)	66.30	0.28	56	0.62	1.10	16.72	7.43	1.10	1.95	599	0.06	0.46	3.44	78.28	8.25	0.39	–	0.07	1111	183
		SD	0.24	0.04	7	0.20	0.31	5.46	1.45	0.30	1.19	39	0.07	0.19	3.32	13.65	8.59	0.09	–	0.02	77	9
		Min	66.01	0.25	47	0.37	0.49	8.81	5.13	0.75	0.65	528	0.02	0.20	0.25	61.65	0.36	0.31	–	0.06	1031	163
	Dark brown, vein	Max	66.61	0.38	68	0.98	1.49	27.74	9.44	1.46	4.79	641	0.21	0.81	9.48	109.66	28.28	0.49	–	0.09	1258	196
		Mean (10)	63.14	2.75	137	12.56	3.08	13.05	7.83	1.32	1.66	728	0.79	0.31	2.09	26.56	9.33	–	2.45	–	868	253
		SD																				

(continued on next page)

Table 4 (continued)

		Zn (%)	Fe (%)	Mn	Co	Ni	Cu	Ga	Ge	Ag	Cd	In	Sn	Sb	Hg	Pb	As	Se	Tl	Zn/ Cd	Temperature	
4101-16		Mean (6)																				
		SD	0.29	0.16	22	2.15	1.33	2.03	0.37	0.31	0.75	17	0.08	0.17	2.77	2.54	10.24	-	0.45	-	22	2
		Min	62.86	2.61	93	10.39	1.39	11.02	7.48	0.97	0.77	705	0.71	0.12	0.44	24.06	2.51	-	2.14	-	836	251
		Max	63.56	3.00	151	14.97	4.73	16.48	8.51	1.73	2.81	752	0.95	0.61	7.00	30.86	29.38	-	2.77	-	892	255
4101-74	Yellow brown, vein-breccia	Mean (15)	64.89	1.10	232	7.20	4.74	18.07	6.48	1.04	3.29	1281	0.26	3.11	4.36	120.54	15.50	1.06	3.61	-	507	246
		SD	0.39	0.11	22	2.65	1.19	4.55	1.35	0.27	1.62	48	0.07	2.23	5.86	15.10	20.57	0.81	-	-	19	6
		Min	64.42	0.99	190	4.63	3.50	11.65	4.27	0.78	1.52	1193	0.16	1.00	0.78	99.53	2.34	0.34	3.61	-	482	235
		Max	65.63	1.29	278	11.27	7.95	31.07	8.54	1.44	8.05	1348	0.39	10.23	24.67	160.40	87.71	1.94	3.61	-	543	257
4101-100	Brown, vein	Mean (8)	63.94	1.98	226	1.32	3.79	19.74	14.65	0.97	1.62	840	0.14	0.29	1.12	39.19	3.84	-	3.89	0.04	761	238
		SD	0.13	0.01	4	0.05	0.90	3.10	2.29	0.06	1.03	23	0.02	0.17	0.50	3.07	4.68	-	0.70	-	20	3
		Min	63.76	1.96	221	1.23	2.48	13.93	10.78	0.85	0.93	812	0.11	0.09	0.56	33.60	0.46	-	2.81	0.04	730	234
		Max	64.17	2.00	235	1.41	5.40	22.48	16.91	1.05	3.95	875	0.17	0.42	1.55	43.47	11.45	-	4.89	0.04	787	242
4101-103	Pale yellow, vein	Mean (8)	66.37	0.56	110	3.31	4.73	12.76	8.17	0.77	2.55	794	0.03	0.26	0.53	56.63	4.90	0.51	1.44	-	836	208
		SD	0.06	0.01	7	0.36	0.53	1.82	0.26	0.15	1.26	10	0.01	0.25	0.47	2.26	5.69	-	-	-	10	5
		Min	66.28	0.54	104	2.94	3.72	11.00	7.61	0.66	1.53	784	0.02	0.10	0.22	52.89	0.69	0.51	1.44	-	818	202
		Max	66.42	0.58	123	3.91	5.21	16.87	8.50	1.03	5.56	812	0.05	0.86	1.24	59.41	18.32	0.51	1.44	-	847	215
4101-104	Pale yellow, disseminated	Mean (6)	65.69	0.46	143	0.22	0.49	13.91	9.15	0.98	2.67	542	0.02	0.22	1.77	80.98	9.87	0.50	1.80	-	1214	198
		SD	0.41	0.01	5	0.08	0.10	0.94	0.43	0.12	1.22	16	0.01	0.06	1.12	7.28	6.25	-	0.19	-	38	11
		Min	65.51	0.45	138	0.13	0.41	12.67	8.43	0.84	1.49	524	0.01	0.18	0.45	70.58	1.81	0.50	1.65	-	1165	187
		Max	66.52	0.47	152	0.32	0.60	15.27	9.63	1.07	4.73	563	0.02	0.26	3.07	87.66	17.32	0.50	2.02	-	1251	211
4101-105	Pale yellow, massive	Mean (10)	65.81	0.72	121	0.70	0.63	12.42	3.57	1.45	3.79	771	0.06	0.24	1.58	76.62	17.29	0.61	2.55	-	859	220
		SD	0.50	0.08	15	0.27	0.08	3.88	0.42	0.41	2.73	62	0.04	0.13	1.53	9.18	17.60	0.19	-	-	72	8
		Min	65.11	0.56	92	0.36	0.51	7.61	2.54	0.75	1.21	691	0.01	0.12	0.21	64.11	1.18	0.48	2.55	-	743	207
		Max	66.36	0.81	142	1.07	0.76	20.37	3.95	1.85	9.65	886	0.11	0.41	4.92	93.17	54.58	0.75	2.55	-	958	235
4101-120	Dark brown, massive	Mean (7)	62.51	3.14	247	31.17	0.94	13.03	5.10	1.32	4.68	1396	0.83	0.35	5.45	30.14	19.69	-	3.62	0.03	448	266
		SD	0.36	0.11	11	1.35	0.28	3.86	0.54	0.17	3.84	55	0.60	0.22	4.61	1.02	13.63	-	0.79	-	17	7
		Min	62.20	3.02	232	29.67	0.49	9.86	4.35	1.08	1.49	1322	0.30	0.17	0.62	28.27	2.05	-	2.68	0.02	423	258
		Max	63.27	3.26	261	32.93	1.33	20.92	5.62	1.52	12.75	1478	1.49	0.77	14.81	31.34	45.60	-	4.95	0.03	470	274
4101-133	Dark brown, vein	Mean (6)	59.41	5.51	221	148.35	0.36	20.25	1.34	1.44	2.13	1158	4.39	0.40	0.39	12.21	6.75	-	6.34	-	520	302
		SD	0.58	0.51	59	9.36	0.02	29.32	0.41	0.24	0.82	135	2.75	-	0.33	5.25	7.69	-	1.40	-	70	4
		Min	58.61	4.95	105	131.25	0.34	6.67	0.55	1.24	1.46	923	2.42	0.40	0.22	7.07	1.81	-	4.30	-	458	298
		Max	59.99	6.12	275	155.98	0.37	80.06	1.74	1.82	3.48	1295	9.89	0.40	0.98	20.87	22.23	-	8.19	-	650	309
H3102	Pale yellow, massive	Mean (7)	66.17	0.45	111	0.48	0.65	16.61	12.10	0.93	2.59	771	0.10	0.85	1.90	121.70	1.40	0.93	7.22	0.05	859	205
		SD	0.10	0.01	8	0.19	0.13	3.47	1.55	0.24	1.93	33	0.05	0.49	2.18	7.18	1.60	0.17	-	-	39	5
		Min	66.02	0.44	103	0.32	0.45	12.28	10.36	0.71	1.27	726	0.06	0.39	0.66	108.66	0.26	0.81	7.22	0.05	819	195
		Max	66.28	0.46	121	0.73	0.81	22.05	14.17	1.28	6.88	806	0.18	1.86	5.78	129.90	4.95	1.05	7.22	0.05	913	210
H3103	Pale yellow, massive	Mean (7)	65.85	0.58	93	0.52	0.92	55.03	40.70	1.56	6.97	1365	1.25	1.33	6.81	127.79	32.50	0.52	3.46	-	484	203
		SD	0.33	0.01	4	0.15	0.26	8.90	5.98	0.21	3.75	69	0.08	0.52	3.40	7.07	47.78	0.12	0.61	-	23	8
		Min	65.43	0.57	89	0.33	0.49	41.52	34.96	1.29	2.94	1305	1.15	0.60	2.75	119.46	3.28	0.39	2.74	-	447	195
		Max	66.31	0.59	99	0.68	1.21	69.16	50.88	1.75	12.89	1472	1.39	1.93	12.57	140.48	125.18	0.70	4.27	-	504	216
H3104	Pale yellow, massive	Mean (7)	65.82	0.60	62	0.47	1.09	45.55	35.68	1.57	2.18	1277	1.44	1.14	1.36	135.47	1.82	0.73	4.10	-	516	199
		SD	0.27	0.02	5	0.16	0.30	7.82	7.49	0.24	0.79	56	0.26	0.18	0.98	4.91	1.06	-	-	-	22	5
		Min	65.48	0.58	55	0.24	0.78	31.24	23.39	1.13	1.50	1217	1.12	0.87	0.24	128.52	0.30	0.73	4.10	-	485	193
		Max	66.08	0.62	72	0.61	1.56	56.72	43.61	1.78	3.90	1359	1.92	1.35	3.13	144.33	3.78	0.73	4.10	-	540	210
H840	Pale yellow, massive	Mean (7)	66.18	0.49	67	0.77	0.36	20.66	13.64	0.68	1.54	1112	0.30	1.06	1.45	88.22	7.99	0.41	-	-	596	208
		SD	0.21	0.01	8	0.14	0.06	3.18	1.88	0.12	0.67	31	0.05	0.53	1.90	4.75	17.36	-	-	-	17	4
		Min	65.72	0.48	55	0.59	0.32	18.08	11.25	0.58	1.02	1070	0.22	0.52	0.20	83.04	0.29	0.41	-	-	568	204
		Max	66.33	0.50	75	0.97	0.46	27.30	16.53	0.88	2.77	1157	0.36	2.01	5.44	96.90	47.25	0.41	-	-	619	214

Note: Avg. DL = average detection limit; SD = standard deviation; Number in bracket refers to the number of analyses; Temperature: calculated using GGIMFis geothermometer (Frenzel et al., 2016); concentrations below detection limits were assigned arbitrary values of half the detection limits.

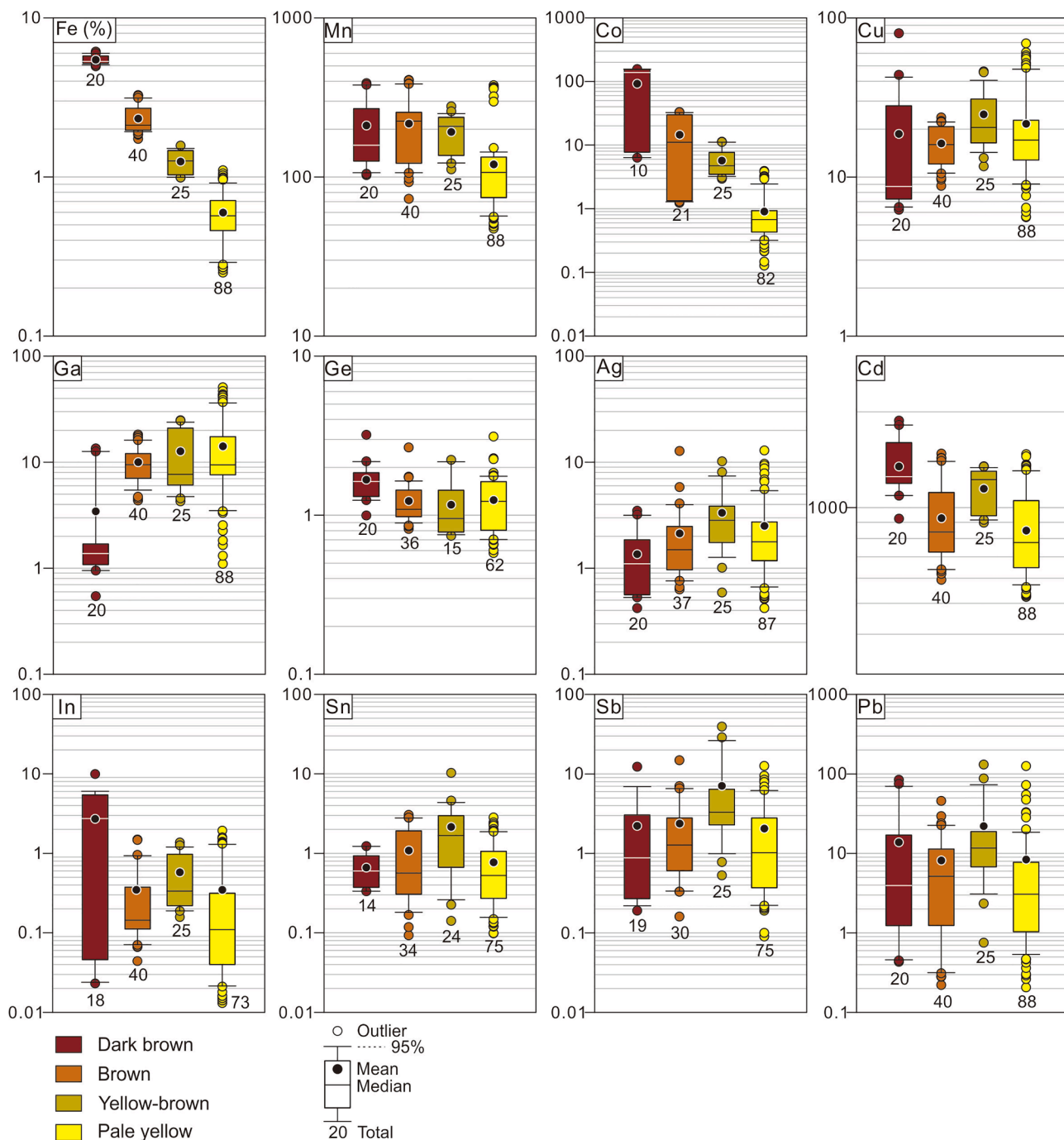


Fig. 9. Box and whisker plots illustrating the trace element variation in sphalerite of varying color at Haerdaban.

2005). However, pyrite 4 has lower abundance of most trace elements, except Ni and Sb, which show high contents (up to 1344.95 ppm, 777.5 ppm, respectively). In particular, the anomalously low As content (BDL to 24.4 ppm) in pyrite 4 stands in contrast to the other pyrite types (40.2 to 4855.27 ppm). This could be explained by the partitioning of trace elements into the coprecipitating sphalerite or other sulfides and carbonates, which lead to significant depletion of most elements in pyrite.

Variable compositions observed in different pyrite types reveal multiple processes for precipitation and modification of pyrite. It has been demonstrated by previous studies (e.g., Huston et al., 1995; Large et al., 2007) and our observations (Fig. 8) that even after significant hydrothermal alteration, As, Ni, and Co are held strongly by the pyrite, due to the nonstoichiometric substitution of As and stoichiometric

substitution of Ni and Co, respectively. The contents of Co, Ni and Co/Ni ratios in pyrite are thus effective discriminants of different genetic types of pyrite (Loftus-Hills and Solomon, 1967; Campbell and Ethier, 1984; Bralía et al., 1979). It has been found that volcanogenic pyrite generally has 400–2400 ppm cobalt and Co/Ni ratios greater than 1 to 2, or between 5 and 50, whereas sedimentary pyrite has <100 ppm cobalt and a Co/Ni value of <1 and hydrothermal pyrite has Co/Ni values range 1–5 (e.g., Loftus-Hills and Solomon, 1967; Bralía et al., 1979). At Haerdaban, the content of Co (0.1–283.91 ppm) and Ni (0.48–300.35 ppm) and Co/Ni ratio (0.01–1.94) of porous pyrite are in the range of sedimentary pyrite (Fig. 11). The comparable Ni, and Co content between overgrowths and cores indicated that the pyrite overgrowths seem to have inherited the trace element signature of the porous pyrite host. The

**Table 5**  
Summary of sulfur isotope values ( $\delta^{34}\text{S}_{\text{V-CDT}}$ ) for pyrite, sphalerite and galena from the Haerdaban deposit as measured by in situ LA-ICP-MS analyses.

Sample	Mineral	Description	N	Mean	SD	Min	Max
3701-6	pyrite	Inclusion-rich, associated with sphalerite	8	15.0	0.5	13.9	15.6
	pyrite	Euhedral	5	15.5	0.5	14.7	16.0
	sphalerite	Dark brown, massive	7	16.4	0.4	15.7	16.9
3701-25	pyrite	Euhedral	4	10.1	0.3	9.8	10.4
	pyrite	Inclusion-rich, associated with sphalerite	4	9.6	0.0	9.6	9.7
3701-27	sphalerite	Dark brown, vein	6	10.0	0.2	9.8	10.3
	pyrite	Porous core	12	5.2	1.3	3.9	8.1
	pyrite	Overgrowth	12	14.4	2.8	8.0	16.4
	sphalerite	Brown, massive	7	15.3	0.5	14.6	15.8
3701-28	sphalerite	Pale yellow, massive	3	16.4	0.3	16.2	16.8
	sphalerite	Yellow brown, vein	9	8.7	0.3	8.4	9.4
	galena	Inclusion in sphalerite	15	7.8	0.4	7.0	8.4
3701-30	pyrite	Euhedral	5	11.0	0.8	10.5	12.5
3701-64	pyrite	Overgrowth	6	16.6	0.2	16.4	16.8
	sphalerite	Brown, massive	4	16.3	0.4	16.0	16.9
3701-96	sphalerite	Pale yellow, massive	4	15.9	1.0	15.3	17.4
3701-97	sphalerite	Pale yellow, massive	4	17.3	0.1	17.1	17.4
3701-112	sphalerite	Pale yellow, massive	3	16.6	1.5	15.7	18.3
4101-16	sphalerite	Dark brown, vein	6	16.7	0.2	16.5	17.0
4101-54	pyrite	Porous core	4	5.2	1.1	4.1	6.5
	pyrite	Overgrowth	3	7.7	0.2	7.5	7.9
4101-74	sphalerite	Yellow brown, vein-breccia	9	12.3	0.7	11.3	13.0
	galena	Vein	4	9.9	0.3	9.7	10.3
4101-100	sphalerite	Brown, vein	6	15.3	0.9	14.5	16.5
4101-103	sphalerite	Pale yellow, vein	6	17.1	0.2	16.9	17.5
4101-104	sphalerite	Pale yellow, disseminated	6	16.3	0.3	16.0	16.9
4101-105	sphalerite	Pale yellow, massive	6	16.2	1.4	14.4	18.2
4101-120	sphalerite	Dark brown, massive	6	14.3	0.4	13.8	14.9
4101-133	pyrite	Inclusion-rich, associated with sphalerite	6	8.5	0.3	8.1	9.0
	sphalerite	Dark brown, vein	6	9.3	0.1	9.2	9.5
4101-151	pyrite	Porous core	3	7.4	1.1	6.4	8.5
	pyrite	Overgrowth	3	10.2	0.1	10.1	10.3
4101-152	pyrite	Porous core	4	8.3	0.4	8.0	8.8
4301-176	pyrite	Overgrowth	4	10.3	0.2	10.0	10.5
	pyrite	Porous core	4	8.3	0.4	7.8	8.7
H3102	pyrite	Overgrowth	4	9.6	0.2	9.4	9.8
	sphalerite	Pale yellow, massive	3	15.6	1.4	13.9	16.6
H3103	sphalerite	Pale yellow, massive	4	17.7	0.1	17.7	17.8
H3104	sphalerite	Pale yellow, massive	3	17.6	0.6	17.0	18.1
	galena	Inclusion in sphalerite	2	16.4	0.4	16.2	16.7
H840	sphalerite	Pale yellow, massive	3	17.1	0.2	16.9	17.2
	galena	Massive	3	16.4	0.2	16.2	16.6

Note: N = number of measurements; SD = standard deviation.

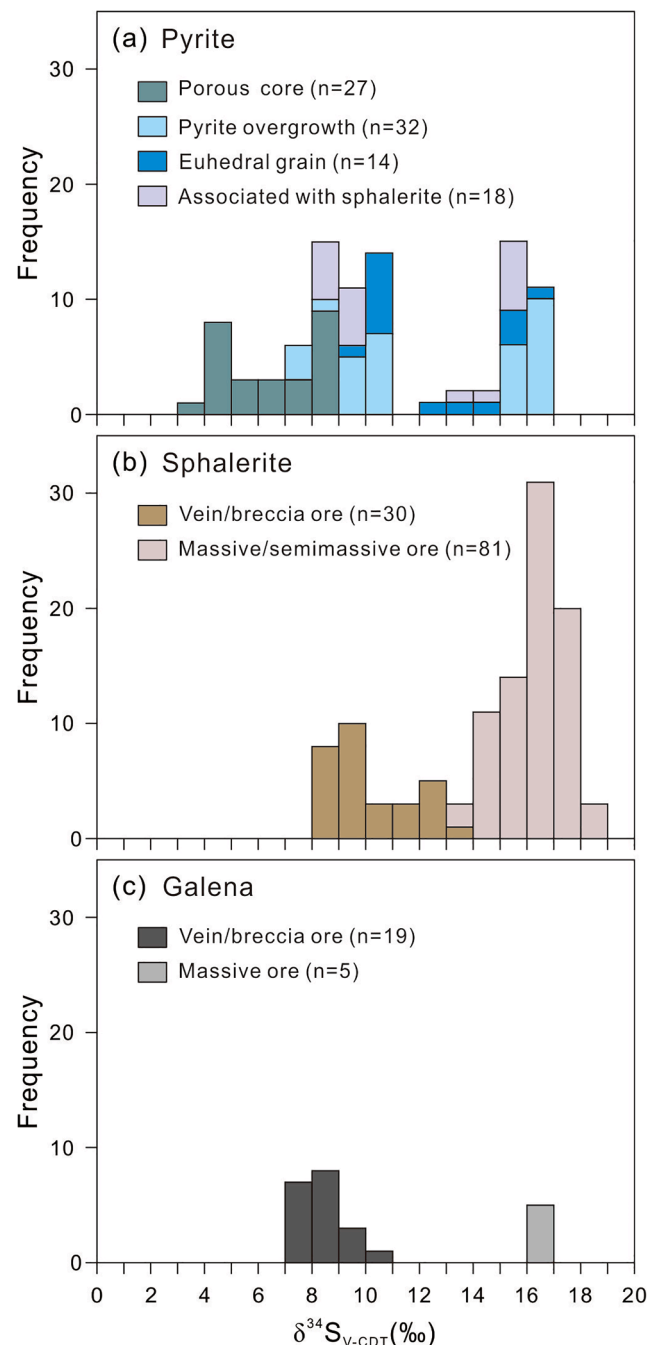


**Fig. 10.** Histogram of sulfur isotope values ( $\delta^{34}\text{S}_{\text{V-CDT}}$ ) for pyrite (a), sphalerite (b) and galena (c) from the Haerdaban deposit.

content of Co (7.52–9491.96 ppm) and Co/Ni ratio (0.62–672.45) for euhedral pyrite are much higher than those in sedimentary pyrite and hence believed to reflect the hydrothermal influence at high temperature (Huston et al., 1995; Maslennikov et al., 2009). The dominance of Ni (24.58–1344.95 ppm) and low contents of Co (usually below detection limit) in pyrite associated with mineralization are typical features of sedimentary pyrite (Fig. 11). This implies that the underlying carbonaceous shales and organic-rich sediments were acting as a source of Ni and other metals for the ore-forming fluids.



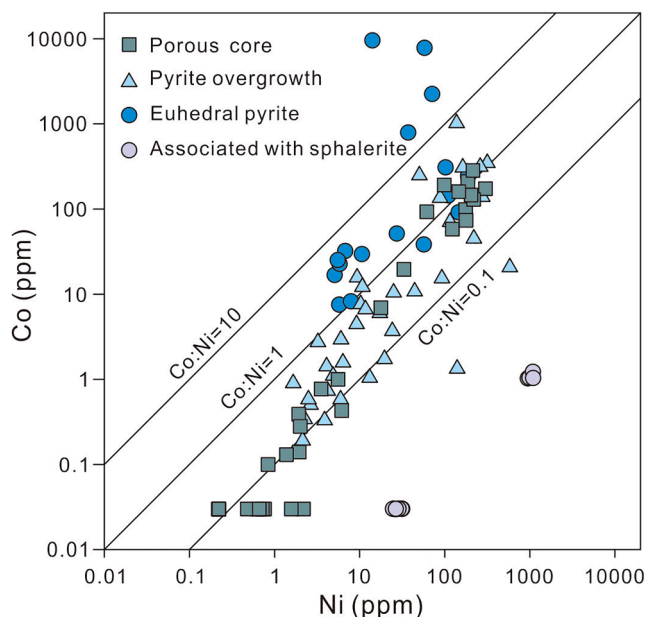


**Fig. 11.** Plot of Co vs. Ni contents of different pyrite types in the Haerdaban deposit. Concentrations below detection limits were assigned values of half the detection limit for data plotting and interpretation.

**6.2. Sphalerite chemical variations and constraint on temperature of mineralization**

Sphalerite can incorporate a wide range of minor and trace elements in its structure, such as Fe, Mn, Cd, Ga, Ge, In, Sn, Co, As, and Tl (e.g., Cook et al., 2009). Their distribution and substitution mechanisms in sphalerite were investigated extensively by previous authors (e.g., Di Benedetto et al., 2005; Cook et al., 2009). Divalent cations, such as Fe<sup>2+</sup>, Mn<sup>2+</sup>, Cd<sup>2+</sup>, and Co<sup>2+</sup>, are readily incorporated into sphalerite through

direct substitution for Zn<sup>2+</sup>, at concentrations up to several weight percent (Lepetit et al., 2003; Di Benedetto et al., 2005; Wright and Gale, 2010). In the Haerdaban deposit, a high negative correlation exists between Zn and Fe in sphalerite within the entire dataset (Fig. 12a), indicating the substitution of Fe<sup>2+</sup> for Zn<sup>2+</sup> in sphalerite is dominant. The direct substitution of Cd<sup>2+</sup>, and Mn<sup>2+</sup> for Zn<sup>2+</sup> are of minor importance as their contents are low in all sphalerite investigated.

The tri- and tetravalent cations, like In<sup>3+</sup>, Ga<sup>3+</sup>, Ge<sup>4+</sup>, and Sn<sup>4+</sup>, usually substitute into sphalerite via coupled substitution with monovalent cations including Cu<sup>+</sup> and Ag<sup>+</sup> (Patrick et al., 1993; Cook et al., 2012; Belissont et al., 2014, 2016; Johan, 1988; Wei et al., 2019). The incorporation of these element in sphalerite at Haerdaban are restricted to low concentrations. Several studies have shown that In concentrations in sphalerite increase with the presence of Cu, following the coupled substitution of 2Zn<sup>2+</sup> ↔ Cu<sup>+</sup> + In<sup>3+</sup> (Cook et al., 2009; Frenzel et al., 2016). However, the In content in sphalerite at Haerdaban is dominantly below 10 ppm, while the Cu content displays a large spread (5.58 to 80.06 ppm), and a positive correlation between them was not observed. Instead, the Cu contents show a positive correlation with Ga (Fig. 12b), indicating the presence of coupled substitution 2Zn<sup>2+</sup> ↔ Cu<sup>+</sup> + Ga<sup>3+</sup> in sphalerite at Haerdaban. The data points plotting above the 1:1 line toward higher Cu contents are mostly related to micro-inclusions of chalcopyrite in sphalerite. Due to the low concentrations, there are no clear correlations between Ge, In and Sn. Nevertheless, a bivariate plot of the total tri- and tetravalent cations vs. total monovalent cations shows that almost all data points plot along the (Cu + Ag)/(In + Ge + Ga + Sn) = 1:1 line (Fig. 12c), supporting the coupled substitution of these elements into sphalerite. In addition, a generally positive correlation between Pb and Sb (Fig. 12d) likely reflect submicroscopic inclusions of Pb tellurides in the sphalerite.

The overall Fe contents (0.25 to 6.12 wt%) in sphalerite at Haerdaban are compatible with that of some SEDEX deposit (commonly 0.5 to 8 wt%) and are much higher than that described for MVT ores, which are usually <0.5 wt% Fe (Cook et al., 2009; Frenzel et al., 2016). The variation in the Fe content strongly correlates with color differences of sphalerite at Haerdaban, with dark-colored (dark brown, brown)

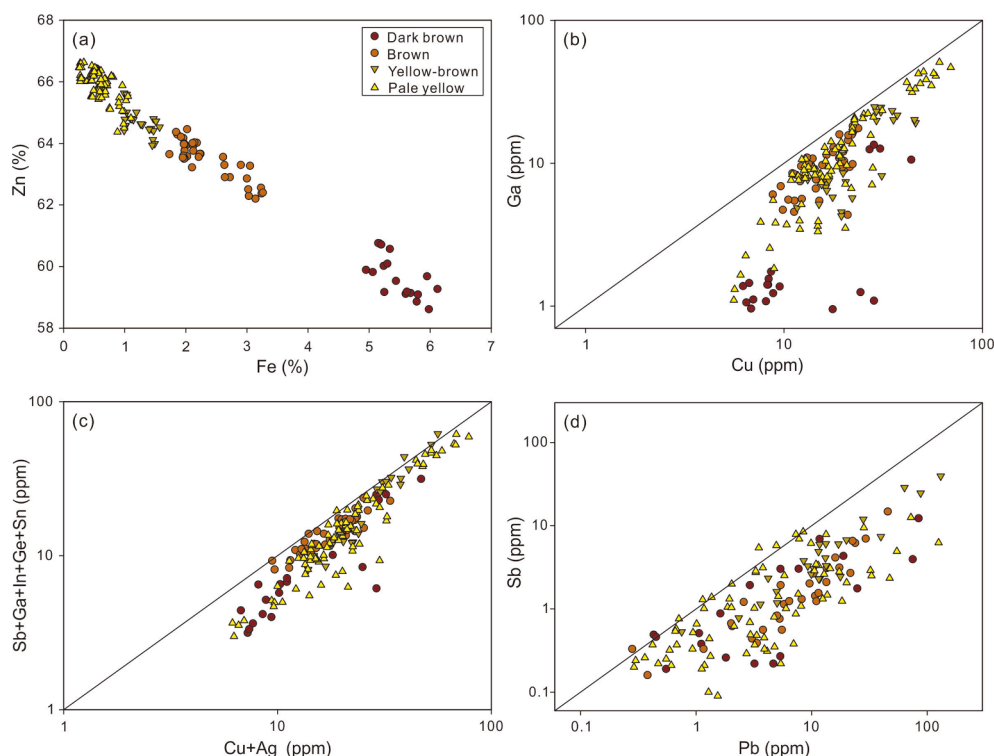


**Fig. 12.** Bivariate plots of concentration of selected trace elements in sphalerite from the Haerdaban deposit. (a) Fe vs. Zn plot showing inverse correlation in sphalerite. (b) A generally positive correlation between Cu and Sb indicating the coupled substitution 2Zn<sup>2+</sup> ↔ Cu<sup>+</sup> + Ga<sup>3+</sup> in sphalerite. (c) A strong correlation between Cu + Ag (monovalent cations) and Sb + Ga + Ge + In + Sn (tri- and tetravalent cations) highlighting the coupled substitution of these elements into sphalerite. (d) A generally positive correlation between Pb and Sb reflecting submicroscopic inclusions of Pb tellurides in the sphalerite.

sphalerite having higher Fe contents relative to the light-colored (yellow–brown, pale yellow) sphalerite (Fig. 9). The variations in Fe between dark-colored and light-colored sphalerite can be interpreted as a result of decreases in temperature and/or increases in sulfur fugacity (e.g., Scott, 1983; Nadoll et al., 2019).

Compared with the high variance of Fe and its close correlation with color variation, the Cd contents vary only slightly throughout the sphalerite types and do not seem to contribute to the coloring effect. The lack of correlation between Cd content and sphalerite color has been observed in some sediment-hosted sulfide deposits. For example, Kelley et al. (2004) reported that Cd contents in sphalerite at Red Dog do not significantly vary among different sphalerite generations, even though contents of other elements (Fe, Co, Mn, Tl and Ge) are highly variable. Cadmium contents in sphalerite are commonly rather uniform in a given deposit (Cook et al., 2009), and seem to be largely controlled by the origin of the ore-forming fluids. The Cd content and Zn/Cd ratio could be used to discriminate sphalerite between different ore deposit (e.g., Gottesmann and Kampe, 2007; Song, 1984). Generally, sphalerite of MVT deposit has high Cd contents (2415 to 34981 ppm, average 9399 ppm) and low Zn/Cd ratios (17 to 201, average 101), whereas sphalerite of SEDEX deposit is characterized by lower Cd contents (595 to 996 ppm, average 832 ppm) and higher Zn/Cd ratios (326 to 368, average 353) (e.g., Lockington et al., 2014; Schwartz, 2000; Ye et al., 2011; Wen et al., 2016). The Cd contents (524–1875 ppm, average 966 ppm) and Zn/Cd ratios (320–1258, average 736) for sphalerite at Haerdaban are compatible with those of SEDEX Zn-Pb deposit.

Trace element concentrations in sphalerite are largely controlled by the composition of ore-forming fluid (Cook et al., 2009; Belissont et al., 2014), but the formation temperature also appears to be a key factor (Frenzel et al., 2016). Previous studies indicated that Fe, Mn, In, Co, and Sn are generally enriched in sphalerite from high-temperature hydrothermal deposit, while Ga, Ge, Se, Tl, and As tend to be more concentrated in low-temperature deposit without a magmatic source (e.g., Cook et al., 2009; Ye et al., 2011; Belissont et al., 2014). The recent meta-analysis of Frenzel et al. (2016) showed that the incorporation of Ga, Ge, In, Mn and Fe in sphalerite are temperature-dependent and their concentrations in sphalerite can be used as a geothermometer (GGIM-Fis). We applied this geothermometer to constrain the formation temperature of sphalerite at Haerdaban. For calculation and statistics, concentrations below detection limits were assigned arbitrary values of half the detection limits. The calculated temperatures range from a minimum of 163 °C to a maximum of 309 °C (Table 4), corresponding to the lighter and darker colored sphalerite sectors, respectively. It is important to note that the dark-colored sphalerite with higher temperature estimates also coincides with the higher Co concentrations (Table 4). As mentioned above, dark-colored sphalerite commonly occurs in veinlet that represent a relatively early formation during the main ore-forming stage. Given these observations, the gradual decrease in temperature from early dark vein sphalerite to late light-colored massive sphalerite was interpreted as evidence for progressive cooling of ore-forming fluid that precipitated contemporaneous sphalerite, galena, and pyrite.

### 6.3. Sources of sulfur

It is widely accepted that seawater sulfate entrapped within sediments and/or connate water is the ultimate source of sulfur in sulfide minerals in sedimentary basin (e.g., Leach et al., 2005; Sangster, 2018). The seawater sulfate could be reduced to H<sub>2</sub>S by several processes, with bacterial sulfate reduction (BSR) and thermochemical sulfate reduction (TSR) are the dominated mechanisms (e.g., Seal, 2006; Hoefs, 2009). The BSR primarily takes place at temperatures lower than 80 °C (Machel et al., 1995), although its occurrence has also been found at temperatures up to 110 °C (Jørgensen et al., 1992). It can cause a large isotope fractionation between H<sub>2</sub>S and sulfate, producing sulfide with highly negative  $\delta^{34}\text{S}$  values in an open system (i.e.,  $\leq -30\text{‰}$ ; Ohmoto and Rye,

1979; Seal, 2006). The TSR commonly occurs at temperatures above 130 °C and result in sulfide with  $\delta^{34}\text{S}$  values 0 to 15‰ lighter than the parent sulfate (Machel et al., 1995; Ohmoto and Goldhaber, 1997).

Previous study on the Haerdaban deposit has reported broad variations in  $\delta^{34}\text{S}$  values from 2.6 to 14.5‰ for sphalerite, 3.8 to 14.9‰ for galena, and 6.5 to 10.3‰ for pyrite from sulfide ores and host rocks (Cheng et al., 2015). The variable  $\delta^{34}\text{S}$  values were interpreted to reflect reduction of seawater sulfate and isotopic disequilibrium between coexisting sulfide minerals in the Haerdaban (Cheng et al., 2015). The in situ  $\delta^{34}\text{S}$  values obtained in this study are consistently positive and vary from +3.9 and +18.3‰, with three dominant modes occurring at 3.9 to 8.8‰, +7.0 to +13.0‰, and +13.8 to +18.3‰ (Fig. 11). These values are broadly similar to the conventional  $\delta^{34}\text{S}$  data for bulk sulfide separates (Cheng et al., 2015). Nevertheless, combining in situ  $\delta^{34}\text{S}$  data with detailed paragenetic and textural observations enable us to better constrain the sources of sulfur for the ore formation.

The porous pyrite core, which was the earliest sulfide phase at Haerdaban, has lower positive  $\delta^{34}\text{S}$  values of 3.9 to 8.8‰ (Fig. 11a). The absence of framboidal or colloform textures (Goldhaber and Kaplan, 1975) and negative  $\delta^{34}\text{S}$  values related to BSR argue against the input of biogenic sulfur in the precipitation of early-stage sulfides. In contrast, the positive  $\delta^{34}\text{S}$  values are compatible with those expected for TSR-derived sulfur but also overlap to some extent with those of magmatic sulfur (Ohmoto and Rye, 1979; Hoefs, 2009). It is difficult to definitively characterize the sulfur source of the early-stage hydrothermal fluid by means of sulfur isotope signatures. However, as discussed above, the high concentrations of epithermal suite elements (Pb, Sb, Ag, Tl, Sn, Cu, Mn; Table 3) in the porous pyrite may reflect a magmatic fluid influence on the hydrothermal system. The lower positive  $\delta^{34}\text{S}$  values associated with the enrichment of epithermal suite elements in the porous pyrite are similar to those found in seafloor hydrothermal systems (e.g., Herzig et al., 1998; Gill et al., 2019; Sherlock et al., 1999; Brueckner et al., 2014), and suggest a potential magmatic input into the early-stage sulfide assemblages. Therefore, we prefer to accept both TSR-derived sulfur and magmatic sulfur as potential contributions of sulfur for pre-ore sulfide precipitation, though the extent of magmatic contribution is difficult to ascertain.

Sulfide from the main-ore stage exhibit two dominant populations of  $\delta^{34}\text{S}$  values: one pronounced population at, and +13.8 to +18.3‰, a second one at +7.0 to +13.0‰ (Table 5; Fig. 11b,c). These values are variable and much higher than those expected for magmatic sulfur, thus precluding a magmatic sulfur source (Ohmoto and Rye, 1979). They are within the range of  $\delta^{34}\text{S}$  values derived by kinetic fractionation during thermochemical sulfate reduction, and suggest that TSR-derived sulfur was responsible for the bulk of mineralization. In addition, the calculated temperature of mineralization based on trace element compositions in sphalerite (Frenzel et al., 2016) is ~200 to 300 °C, favoring the thermochemical reduction of seawater sulfate (Ohmoto and Rye, 1979; Shanks, 2001; Seal, 2006). The  $\delta^{34}\text{S}$  values of sulfide formed via TSR can be estimated from the original sulfur isotopic composition of the seawater sulfate and temperature (Seal, 2006). The presence of barite at Haerdaban indicate that the TSR occurred in an open system and the sulfate (SO<sub>4</sub>) was continuously replenished (i.e., assuming that  $f = 1$ ). The  $\delta^{34}\text{S}$  value of the initial seawater sulfate at the time of sulfide deposition was taken as the mean value ( $\delta^{34}\text{S} = +33.2\text{‰}$ , our unpublished data) of barite in the deposit. Using the equations outlined in Ohmoto and Rye (1979), the calculated  $\delta^{34}\text{S}$  values at temperatures of 163 and 309 °C range from 8.0 to 19.0‰ for pyrite, 6.5 to 18.1‰ for sphalerite, and 2.6 to 15.9‰ for galena, broadly overlapping with the measured values. This suggest that TSR can account for the isotopic composition of sulfides of the semi-massive to massive ores.

However, the calculated value ( $\delta^{34}\text{S} = \sim +18\text{‰}$ ) at elevated temperature (300 °C) is much higher than the measured values ( $\delta^{34}\text{S} = +7.0$  to +13.0‰) of sulfide in veins. In particular, the trend of increasing  $\delta^{34}\text{S}$  values in sulfide with decreasing temperature cannot be explained simply by TSR as a sole source, because TSR will produce sulfide with

heavy  $\delta^{34}\text{S}$  values at high temperature (Ohmoto and Rye, 1979). Therefore, mixing of TSR-derived sulfur with an additional source of sulfur with lower  $\delta^{34}\text{S}$  values is required to produce the range of  $\delta^{34}\text{S}$  values observed in the vein ores. The potential source for the isotopically light sulfur is the diagenetic pyrite with lower  $\delta^{34}\text{S}$  values (+3.8 to +8.9‰) in carbonate-clastic rocks of the Haerdaban Formation. Diagenetic pyrite is relatively minor, but is widespread throughout the entire succession. Textural observations of irregular boundaries between pyrite overgrowths and remnant of earlier pyrite (Fig. 4a,b) indicate that some of the pyrite were dissolved during recrystallization and therefore provided sulfur for the formation of pyrite overgrowth and associated sulfide. Additional evidence for extraction of sulfur and metals from host rocks comes from the enrichments of Mn, Co, and Ni in sphalerite in the veins, because the pyrite and sedimentary matrix are enriched in these elements.

Taking these data into consideration, sulfur isotope compositions ( $\delta^{34}\text{S} = +3.8$  to +8.9‰) for the earlier porous pyrite cores likely originate from thermochemical sulfate reduction (TSR) with a possible contribution of magmatic sulfur source, given the association of lower positive  $\delta^{34}\text{S}$  values and enrichment of epithermal suite elements in the porous pyrite. The dominant population with heavier  $\delta^{34}\text{S}$  values (+13.8 to +18.3‰) recorded in the sulfide in massive ores support a sulfur reservoir derived via TSR for the main-stage mineralization. The intermediate  $\delta^{34}\text{S}$  values (+7.0 to +13.0‰) of sulfide from vein ores are most likely a mixing of TSR-derived sulfur with light sulfur leached from preexisting pyrite during formation of the vein ores.

#### 6.4. Implication for ore genesis

In the Sailimu-Tekeli area, sediment-hosted Pb-Zn deposits are often hosted within the Proterozoic carbonate-clastic sediments and have been moderately metamorphosed during the Paleozoic accretionary orogenesis. In contrast to the laminated sulfide ores pervasively met in the adjacent Tuokesai deposit (Man et al., 2020) and other typical SEDEX deposits (Sangster, 2002; Large et al., 1998; Leach et al., 2005; Goodfellow and Lydon, 2007; Wilkinson, 2014), stratabound but discordant vein-breccias sulfide ores are dominated at Haerdaban,

indicating that mineralization occurred after sedimentation and diagenesis. The complex ore textures and uncertainty in exact age of mineralization at Haerdaban, make determining a single robust genetic model difficult. Nevertheless, textural, compositional and isotopic data for sulfides reveal a likely two-stage process for the deposit which involved an early sulfide deposition on the seafloor and a secondary replacement of preexisting ores (Fig. 13).

The mineralization event begins with an early introduction of metals in the sedimentary sequences via hydrothermal exhalation. This was, in part, manifest by the porous pyrite, which have enrichment of ore-forming elements (Pb, Zn, Ag) and epithermal suite of elements (Tl, Sn, Sb) in association with lower positive  $\delta^{34}\text{S}$  values (Fig. 13a). The original size of base metal mineralization of this stage is unclear, as the primary ore textures would have been completely obscured by hydrothermal overprint during the introduction of late-stage fluids. At current levels of exploration, laminated sulfide ore was not well developed, and only minor disseminated or matrix sphalerite were observed in the host rocks. The precipitation of sulfide ores via sedimentary exhalation is well exemplified by the Tuokesai deposit (Man et al., 2020), which lies in the close vicinity of the Haerdaban district, about 10 km to the north. The similar sulfur isotope compositions of sulfide from Haerdaban and Tuokesai ( $\delta^{34}\text{S} = +8.1$  to +20.4‰; Man et al., 2020) indicate a common source of sulfur from TSR for both deposits. It is possible that formation of ores from an exhalative hydrothermal solution may also have occurred at Haerdaban.

The hydrothermal stage involved the formation of dolomite in close association with Zn-Pb ores. The pervasive zebra dolomite and dolomite vein-breccias in the district suggests that hot hydrothermal brines (~10–25 wt% NaCl equiv; Diehl et al., 2010) was active during this time. The continued flow of hydrothermal brines caused thermal alteration of carbonaceous limestone and calcareous slate that led to fluid overpressuring, hydrofracturing, and vein formation (Fig. 13b). Early Fe-rich sphalerite precipitated in the veins at temperatures of ~300 °C, accompanied by recrystallization of pyrite. Textural observations and isotopic data show that preexisting sulfide was partly dissolved, providing light sulfur for the precipitation of sulfide along fracture networks of the host rocks. It was suggested that the dark-colored

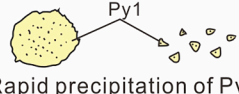
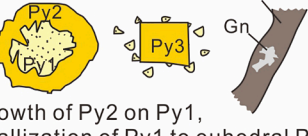
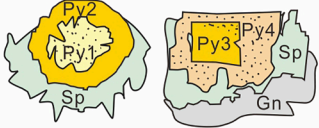
Stages of mineralization	Textural and geochemical features		
	Pyrite	Sphalerite	Galena
Stage I: sedimentation to diagenesis  Rapid precipitation of Py1	Py1: porous, inclusion-rich enriched in Sb, Se, Tl, Ba, Mn, Pb, As, Cu, Ag, Sn $\delta^{34}\text{S} = +3.9$ to +8.8‰		
Stage II: vein mineralization  Overgrowth of Py2 on Py1, recrystallization of Py1 to euhedral Py3	Py2/Py3: inclusion-free, enriched in Co, As±Ni depleted in most trace elements Py2: $\delta^{34}\text{S} = +7.5$ to +16.8‰ Py3: $\delta^{34}\text{S} = +9.8$ to +16.0‰	Vein-hosted, dark-colored enriched in Fe, Co, In $\delta^{34}\text{S} = +8.4$ to +13.0‰	Inclusion in sphalerite $\delta^{34}\text{S} = +7.0$ to +10.3‰
Stage II: main mineralization  Rapid precipitation of Py4, co-precipitation of sphalerite	Py4: inclusion-rich enriched in Ni, Sb depleted in most trace elements $\delta^{34}\text{S} = +8.1$ to +15.6‰	Massive, light-colored enriched in Ga $\delta^{34}\text{S} = +13.8$ to +18.3‰	Open space fillings $\delta^{34}\text{S} = +16.2$ to +16.7‰

Fig. 13. Schematic diagram showing the textural, trace element and sulfur isotope variations in sulfide from the Haerdaban deposit.



sphalerite vein-breccias represent pathways for the hydrothermal brines that formed the massive ores.

Sulfur isotope composition of main-stage sulfide is consistent with a seawater sulfate source without any significant magmatic sulfur input in this stage (Fig. 13c). The origin of low-temperature base metal deposits in the limestones is mostly connected with basinal brines. The circulation of basinal brines within the thick package of carbonaceous and sulfidic black slate of the Haerdaban Group would lead to the extraction of Zn and Pb mainly as chloride complexes (Hanor, 1996; Reed and Palandri, 2006). The metalliferous fluids that migrate upward along fault systems and then interact with the sedimentary rocks should precipitate sulfides very efficiently. This is because an increase in fluid pH due to reaction with the carbonaceous host rocks, will induce a dramatic drop in the solubility of base metals and cause efficient precipitation of sulfide (Seward and Barnes, 1997). Besides fluid neutralization, the significant cooling of the metalliferous fluids was also a major cause of sulfide precipitation.

Based on the geological evidence, ore texture, trace element and sulfur isotope signatures of sulfide, it seems logical to classify Haerdaban deposit as a modified SEDEX Zn-Pb deposit. After an early introduction of metals by exhalative venting, the main mineralization likely occurred through remobilization and upgrading of earlier ores during hydrothermal events, resulting in chaotic textures, irregular veins and brecciation in the deposit. The modification of the deposit is probably linked to a constant heat flow and hydrothermal activity during the Paleozoic orogeny. Further investigations are required to precisely determine if there is an economic Zn-Pb mineralization during sedimentation and which process is responsible for the modification of the deposit.

## 7. Conclusions

This study has demonstrated the variations in texture, composition and sulfur isotope for sulfide from the sediment-hosted Haerdaban Zn-Pb deposit in the Sailimu terrane (NW China). The results allow distinction of four different pyrite types. The high contents of Mn, Sb, Tl, Ba, Zn, Pb, Ag, Cu in porous pyrite (Py1) indicates an early introduction of base metals into the deposit during sedimentation. The enrichment of Co and As, and depletion of most trace element in the pyrite overgrowths (Py2) and euhedral pyrite (Py3) is attributed to the release of trace elements from pyrite during recrystallization from a porous to massive texture. The dominance of Ni in Pyrite (Py4) from main-stage ores indicates the underlying carbonaceous sediments as a source of Ni and other metals for the ore-forming fluids.

Sphalerite displays a wide variety of colors from dark brown to pale yellow, primarily related to variation in composition. The overall Fe contents (0.25 to 6.12 wt%), Cd contents (524–1875 ppm, average 966 ppm) and Zn/Cd ratios (320–1258, average 736) in sphalerite at Haerdaban are compatible with those of SEDEX Zn-Pb deposit. Calculated temperatures using trace element contents in sphalerite (GGIMFis geothermometer) range from 163 °C to 309 °C, indicating progressive cooling of ore-forming fluid.

In situ LA-MC-ICP-MS analyses of pyrite, sphalerite and galena yield a wide range of  $\delta^{34}\text{S}$  values from +3.9 to +18.3‰. The association of isotopically light sulfur ( $\delta^{34}\text{S} = +3.9$  to +8.8‰) and epithermal suite elements in the porous pyrite indicate that the sulfur was derived from thermochemical sulfate reduction (TSR) with a possible contribution of magmatic sulfur. The heavier  $\delta^{34}\text{S}$  values (+13.8 to +18.3‰) of massive sulfide support a sulfur source derived via TSR for the main mineralization. The intermediate  $\delta^{34}\text{S}$  values (+7.0 to +13.0‰) of vein sulfide are likely a mixing of TSR-derived sulfur with light sulfur leached from diagenetic pyrite. These data suggest that the main-stage ores at Haerdaban were formed by remobilization and upgrading of early exhalative ores through hydrothermal process. The Haerdaban is considered to be a metamorphosed SEDEX Zn-Pb deposit.

## Declaration of Competing Interest

The authors declare that they have no known competing financial interests or personal relationships that could have appeared to influence the work reported in this paper.

## Acknowledgments

We kindly thank Dr. Kaiyun Chen for assistance with LA-MC-ICP-MS sulfur isotope analyses, and Dr. Zhenyu Chen for EPMA analyses. The Xinjiang Institute of Geological Exploration for Nonferrous Resources is acknowledged for access to data and support for field work. We are grateful to the associate editor, Prof. Wenjiao Xiao, and two anonymous reviewers for their thorough and constructive comments, which greatly improved the paper. This research was funded by the National Key Research and Development Program of China (2017YFC0601201), the National Natural Science Foundation of China (grants 41502088), and the National Nonprofit Institute Research Grant of CAGS-IMR (K1608).

## Appendix A. Supplementary data

Supplementary data to this article can be found online at <https://doi.org/10.1016/j.oregeorev.2021.104527>.

## References

- Allen, M.B., Windley, B.F., Zhang, C., 1992. Palaeozoic collisional tectonics and magmatism of the Chinese Tien Shan, central Asia. *Tectonophysics* 220, 89–115.
- Bao, Z., Chen, L., Zong, C., Yuan, H., Chen, K., Dai, M., 2017. Development of pressed sulfide powder tablets for in situ sulfur and lead isotope measurement using LA-MC-ICP-MS. *Int. J. Mass Spectrom.* 421, 255–262.
- Barrie, C.D., Boyce, A.J., Boyle, A.P., Williams, P.J., Blake, K., Wilkinson, J.J., Lowther, M., McDermott, P., Prior, D.J., 2009. On the growth of colloform textures: a case study of sphalerite from the Galmoy ore body, Ireland. *J. Geol. Soc.* 166, 563–582.
- Belissant, R., Boiron, M.-C., Luais, B., Cathelineau, M., 2014. LA-ICP-MS analyses of minor and trace elements and bulk Ge isotopes in zoned Ge-rich sphalerites from the Noailhac – Saint-Salvy deposit (France): Insights into incorporation mechanisms and ore deposition processes. *Geochim. Cosmochim. Acta* 126, 518–540.
- Belissant, R., Muñoz, M., Boiron, M.-C., Luais, B., Mathon, O., 2016. Distribution and oxidation state of Ge, Cu and Fe in sphalerite by  $\mu$ -XRF and K-edge  $\mu$ -XANES: insights into Ge incorporation, partitioning and isotopic fractionation. *Geochim. Cosmochim. Acta* 177, 298–314.
- Biske, Y.S., Seltmann, R., 2010. Paleozoic Tian-Shan as a transitional region between the Rheic and Urals-Turkestan oceans. *Gondwana Res.* 17, 602–613.
- Bralia, A., Sabatini, G., Troja, F., 1979. A reevaluation of the Co/Ni ratio in pyrite as geochemical tool in ore genesis problems. *Miner. Deposita* 14, 353–374.
- Brueckner, S.M., Piercey, S.J., Sylvester, P.J., Maloney, S., Pilgrim, L., 2014. Evidence for syngenetic precious metal enrichment in an appalachian volcanogenic massive sulfide system: the 1806 Zone, Ming Mine, Newfoundland. *Canada. Econ. Geol.* 109, 1611–1642.
- Butler, L.B., Rickard, D., 2000. Framboidal pyrite formation via the oxidation of iron (II) monosulfide by hydrogen sulphide. *Geochim. Cosmochim. Acta* 64, 2665–2672.
- Campbell, F.A., Ethier, V.G., 1984. Nickel and cobalt in pyrrhotite and pyrite from the Faro and Sullivan orebodies. *Can. Mineral.* 22, 503–506.
- Chen, L., Chen, K., Bao, Z., Liang, P., Sun, T., Yuan, H., 2017. Preparation of standards for in situ sulfur isotope measurement in sulfides using femtosecond laser ablation MC-ICP-MS. *J. Anal. At. Spectrom.* 32, 107–116.
- Cheng, Y., Li, Y., Zhu, S.S., Yu, Y.L., 2015. Geological characteristics and genesis analysis of the Haerdaban lead-zinc deposit, Wenquan, Xinjiang. *Mineral Explor.* 6, 107–114 (in Chinese with English abstract).
- Cheng, Y., Yan, C.X., Yu, Y.L., Zhu, S.S., 2011. Geological characteristics and mineral prospect analysis of the Tuokesai lead-zinc ore deposit in Wenquan county, Xinjiang autonomous region. *Miner. Resour. Geol.* 25 (6), 481–484 (in Chinese with English abstract).
- Cook, N.J., Ciobanu, C.L., Brugger, J., Etschmann, B., Howard, D.L., de Jonge, M.D., Ryan, C., Paterson, D., 2012. Determination of the oxidation state of Cu in substituted Cu–In–Fe-bearing sphalerite via  $\mu$ -XANES spectroscopy. *Am. Mineral.* 97, 476–479.
- Cook, N.J., Ciobanu, C.L., Pring, A., Skinner, W., Shimizu, M., Danyushevsky, L., Saini-Eidukat, B., Melcher, F., 2009. Trace and minor elements in sphalerite: a LA-ICPMS study. *Geochim. Cosmochim. Acta* 73, 4761–4791.
- Danyushevsky, L., Robinson, P., Gilbert, S., Norman, M., Large, R., McGoldrick, P., Shelley, M., 2011. Routine quantitative multi-element analysis of sulphide minerals by laser ablation ICP-MS: Standard development and consideration of matrix effects. *Geochem. Explor. Environ. Anal.* 11, 51–60.
- Deditius, A.P., Utsunomiya, S., Reich, M., Kesler, S.E., Ewing, R.C., Hough, R., Walshe, J., 2011. Trace metal nanoparticles in pyrite. *Ore Geol. Rev.* 42, 32–46.



- Degtyarev, K., Yakubchuk, A., Tretyakov, A., Kotov, A., Kovach, V., 2017. Precambrian geology of the Kazakh Uplands and Tien Shan: an overview. *Gondwana Res.* 47, 44–75.
- Di Benedetto, F., Bernardini, G.P., Costagliola, P., Plant, D., Vaughan, D.J., 2005. Compositional zoning in sphalerite crystals. *Am. Mineral.* 90, 1384–1392.
- Diehl, S.F., Hofstra, A.H., Koenig, A.E., Emsbo, P., Christiansen, W., Johnson, C., 2010. Hydrothermal zebra dolomite in the Great Basin, Nevada—attributes and relation to Paleozoic stratigraphy, tectonics, and ore deposits. *Geosphere* 6, 663–690.
- Duan, S.G., 2011. **Regional Metallogenic Regularity and Prospecting Direction of Sailimu Micro-massif, Western Tianshan, China.** Ph.D. thesis, China University of Geosciences (Beijing), Beijing, China, 210 pp. (in Chinese with English abstract).
- Frenzel, M., Hirsch, T., Gutzmer, J., 2016. Gallium, germanium, indium, and other trace and minor elements in sphalerite as a function of deposit type — a meta-analysis. *Ore Geol. Rev.* 76, 52–78.
- Gadd, M.G., Layton-Matthews, D., Peter, J.M., Paradis, S.J., 2016. The world-class Howard's Pass SEDEX Zn-Pb district, Selwyn Basin, Yukon. Part I: trace element compositions of pyrite record input of hydrothermal, diagenetic, and metamorphic fluids to mineralization. *Miner. Deposita* 51, 319–342.
- Gao, J., Maosong, L., Xuchang, X., Yaoqing, T., Guoqi, H., 1998. Paleozoic tectonic evolution of the Tianshan Orogen, northwestern China. *Tectonophysics* 287, 213–231.
- Genna, D., Gaboury, D., 2015. Deciphering the hydrothermal evolution of a VMS system by LA-ICP-MS using trace elements in pyrite: an example from the braccamac-mcleod deposits, Abitibi, Canada, and implications for exploration. *Econ. Geol.* 110, 2087–2108.
- Gill, S.B., Piercey, S.J., Layne, G.D., Piercey, G., 2019. Sulphur and lead isotope geochemistry of sulphide minerals from the Zn-Pb-Cu-Ag-Au Lemarchant volcanogenic massive sulphide (VMS) deposit, Newfoundland, Canada. *Ore Geol. Rev.* 104, 422–435.
- Goldhaber, M.B., Kaplan, I.R., 1975. Controls and consequences of sulfate reduction rates in recent marine sediments. *Soil Sci.* 119, 42–55.
- Goodfellow, W.D., Lydon, J.W., 2007. Sedimentary exhalative (SEDEX) deposits. In: Goodfellow, W.D. (Ed.), **Mineral Deposits of Canada: A Synthesis of Major Deposit Types, District Metallogeny, the Evolution of Geological Provinces, and Exploration Methods:** Geological Association of Canada, Mineral Deposits Division, Special Publication No. 5, pp. 163–183.
- Gottesmann, W., Kampe, A., 2007. Zn/Cd ratios in calcisilicate-hosted sphalerite ores at Tumurtijn-ovoo, Mongolia. *Chem. Erde-Geochem.* 67, 323–328.
- Gu, X.X., Zhang, Y.M., Peng, Y.W., Zhang, L.Q., Wang, X.L., Gao, H., Dong, L.H., Tu, Q.J., 2014. The Fe-Cu-Mo polymetallic mineralization system related to intermediate-acid intrusions in the Boluokenu metallogenic belt of the West Tianshan, Xinjiang: rock-and ore-forming geochemistry and tectonomagmatic evolution. *Earth Sci. Front.* 21, 156–175 (in Chinese with English abstract).
- Han, C., Xiao, W., Su, B., Asamoah Sakyi, P., Ao, S., Zhang, J., Wan, B., Song, D., Zhang, Z., Wang, Z., Xie, M., 2020. Late Paleozoic metallogenesis and evolution of the Chinese Western Tianshan Collage, NW China, Central Asia orogenic belt. *Ore Geol. Rev.* 124, 103643.
- Hanor, J.S., 1996. Controls on the solubilization of lead and zinc in basinal brines. *Soc. Econ. Geol. Special Publication* 4, 483–500.
- He, J., Zhu, W., Zheng, B., Wu, H., Cui, X., Lu, Y., 2015. Neoproterozoic diamicite-bearing sedimentary rocks in the northern Yili Block and their constraints on the Precambrian evolution of microcontinents in the Western Central Asian Orogenic Belt. *Tectonophysics* 665, 23–36.
- Hedenquist, J.W., Lowenstern, J.B., 1994. The role of magmas in the formation of hydrothermal ore deposits. *Nature* 370, 519–527.
- Herzig, P.M., Hannington, M.D., 1995. Polymetallic massive sulfides at the modern seafloor: a review. *Ore Geol. Rev.* 10, 95–115.
- Herzig, P.M., Hannington, M.D., Arribas Jr, A., 1998. Sulfur isotopic composition of hydrothermal precipitates from the Lau back-arc: implications for magmatic contributions to seafloor hydrothermal systems. *Miner. Deposita* 33, 226–237.
- Hoefs, J., 2009. **Stable Isotope Geochemistry.** Springer-Verlag, Berlin, Heidelberg (Germany), p. 285.
- Hu, A.Q., Wei, G.J., Jahn, B.M., Zhang, J.B., Deng, W.F., Chen, L.L., 2010. Formation of the 0.9 Ga Neoproterozoic granitoids in the Tianshan Orogen, NW China: constraints from the SHRIMP zircon age determination and its tectonic significance. *Geochimica* 39, 197–212 (in Chinese with English abstract).
- Huston, D.L., Sie, S.H., Suter, G.F., Cooke, D.R., Both, R.A., 1995. Trace elements in sulfide minerals from eastern Australian volcanic-hosted massive sulfide deposits; Part I, Proton microprobe analyses of pyrite, chalcopyrite, and sphalerite, and Part II, Selenium levels in pyrite; comparison with 834S values and implications for the source of sulfur in volcanogenic hydrothermal systems. *Econ. Geol.* 90, 1167–1196.
- Jochum, K.P., Willbold, M., Raczek, I., Stoll, B., Herwig, K., 2005. Chemical Characterisation of the USGS Reference Glasses GSA-1G, GSC-1G, GSD-1G, GSE-1G, BCR-2G, BHVO-2G and BIR-1G Using EPMA, ID-TIMS, ID-ICP-MS and LA-ICP-MS. *Geostand. Geoanal. Res.* 29, 285–302.
- Johan, Z., 1988. Indium and germanium in the structure of sphalerite: an example of coupled substitution with Copper. *Mineral. Petrol.* 39, 211–229.
- Jørgensen, B.B., Isaksen, M.F., Jannasch, H.W., 1992. Bacterial sulfate reduction above 100°C in deep-sea hydrothermal vent sediments. *Science* 258, 1756–1757.
- Keith, M., Häckel, F., Haase, K.M., Schwarz-Schampera, U., Klend, R., 2016. Trace element systematics of pyrite from submarine hydrothermal vents. *Ore Geol. Rev.* 72, 728–745.
- Keith, M., Smith, D.J., Jenkin, G.R.T., Holwell, D.A., Dye, M.D., 2018. A review of Te and Se systematics in hydrothermal pyrite from precious metal deposits: Insights into ore-forming processes. *Ore Geol. Rev.* 96, 269–282.
- Kelley, K.D., Leach, D.L., Johnson, C.A., Clark, J.L., Fayek, M., Slack, J.F., Anderson, V.M., Ayuso, R.A., Ridley, W.I., 2004. Textural, compositional, and sulfur isotope variations of sulfide minerals in the red dog zn-pb-ag deposits, Brooks Range, Alaska: implications for ore formation. *Econ. Geol.* 99, 1509–1532.
- Large, R., Bull, S., Selley, D., Yang, J., Cooke, D., Garven, G., McGoldrick, P., 2002. Controls on the formation of giant stratiform sediment-hosted Zn-Pb-Ag deposits: with particular reference to the north Australian Proterozoic. In: **Giant Ore Deposits: Characteristics, Genesis, and Exploration Centre for Ore Deposit Research (CODES).** Special Publication 4. University of Tasmania, Australia, pp. 107–149.
- Large, R.R., Bull, S.W., Cooke, D.R., McGoldrick, P.J., 1998. A genetic model for the H.Y. C. Deposit, Australia; based on regional sedimentology, geochemistry, and sulfide-relationship relationships. *Econ. Geol.* 93, 1345–1368.
- Large, R.R., Danyushevsky, L., Hollit, C., Maslennikov, V., Meffre, S., Gilbert, S., Bull, S., Scott, R., Emsbo, P., Thomas, H., Singh, B., Foster, J., 2009. Gold and trace element zonation in pyrite using a laser imaging technique: implications for the timing of gold in orogenic and carlin-style sediment-hosted deposits. *Econ. Geol.* 104, 635–668.
- Large, R.R., Maslennikov, V.V., Robert, F., Danyushevsky, L.V., Chang, Z., 2007. Multistage sedimentary and metamorphic origin of pyrite and gold in the Giant Sukhoi Log Deposit, Lena Gold Province, Russia. *Econ. Geol.* 102, 1233–1267.
- Large, R.R., Meffre, S., Burnett, R., Guy, B., Bull, S., Gilbert, S., Goemann, K., Danyushevsky, L., 2013. Evidence for an intrabasinal source and multiple concentration processes in the formation of the carbon leader Reef, Witwatersrand Supergroup, South Africa. *Econ. Geol.* 108, 1215–1241.
- Leach, D.L., Bradley, D.C., Huston, D., Pisarevsky, S.A., Taylor, R.D., Gardoll, S.J., 2010. Sediment-hosted lead-zinc deposits in earth history. *Econ. Geol.* 105, 593–625.
- Leach, D.L., Sangster, D.F., Kelley, K.D., Large Ross, R., Garven, G., Allen, C.R., 2005. Sediment-hosted Pb-Zn deposits: a global perspective. *Econ. Geol.* 100, 561–608.
- Lepetit, P., Bente, K., Doering, T., Luckhaus, S., 2003. Crystal chemistry of Fe-containing sphalerites. *Phys. Chem. Miner.* 30, 185–191.
- Li, X.D., Qin, Y.Q., 1989. Bortala river fractures and its geotectonic significance. *Xinjiang Geol.* 7 (1), 33–48 (in Chinese with English abstract).
- Liu, C., Xue, C., Chi, G., Zhao, X., Li, Y., 2018. Geology, geochronology and geochemistry of the Dabate Cu-Mo deposit, northern Chinese Tien Shan: Implications for spatial separation of copper and molybdenum mineralization. *Ore Geol. Rev.* 92, 542–557.
- Liu, Y., 2015. **Petrology, Geochemistry and Genesis of Tuokesai Zn-Pb Deposit, Wenquan, Xinjiang.** M.Sc. thesis, China University of Geosciences (Beijing), Beijing, China, 73 pp. (in Chinese with English abstract).
- Lockington, J.A., Cook, N.J., Giobanu, C.L., 2014. Trace and minor elements in sphalerite from metamorphosed sulphide deposits. *Mineral. Petrol.* 108, 873–890.
- Loftus-Hills, G., Solomon, M., 1967. Cobalt, nickel and selenium in sulphides as indicators of ore genesis. *Miner. Deposita* 2, 228–242.
- Machel, H.G., Krouse, H.R., Sassen, R., 1995. Products and distinguishing criteria of bacterial and thermochemical sulfate reduction. *Appl. Geochem.* 10, 373–389.
- Man, R., 2020. **Research on the Proterozoic Zn-Pb Mineralization in Sayram Area, Western Tianshan, NW China.** Ph.D. thesis, China University of Geosciences (Beijing), Beijing, China, 116 pp. (in Chinese with English abstract).
- Man, R., Xue, C., Zhao, X., Liu, Y., Gao, R., Symons, D., 2020. Genesis of the Tuokesai Zn-Pb deposit in the Sayram Massif, Xinjiang, NW China: constraints from geology, jasperite geochemistry and Si-S-Pb isotopes. *Ore Geol. Rev.* 121, 103479.
- Maslennikov, V.V., Maslennikova, S.P., Large, R.R., Danyushevsky, L.V., 2009. Study of trace element zonation in vent chimneys from the silurian yaman-kasy volcanically-hosted massive sulfide deposit (Southern Urals, Russia) using laser ablation-inductively coupled plasma mass spectrometry (LA-ICPMS). *Econ. Geol.* 104, 1111–1141.
- Mukherjee, I., Large, R., 2017. Application of pyrite trace element chemistry to exploration for SEDEX style Zn-Pb deposits: McArthur Basin, Northern Territory, Australia. *Ore Geol. Rev.* 81, 1249–1270.
- Nadol, P., Sošnicka, M., Kraemer, D., Duschl, F., 2019. Post-Variscan structurally-controlled hydrothermal Zn-Fe-Pb sulfide and F-Ba mineralization in deep-seated Paleozoic units of the North German Basin: A review. *Ore Geol. Rev.* 106, 273–299.
- Ohmoto, H., Rye, R.O., 1979. Isotopes of sulfur and carbon. In: Barnes, H.L. (Ed.), **Geochemistry of Hydrothermal Ore Deposits**, second ed. Wiley and Sons, New York, pp. 509–567.
- Paton, C., Hellstrom, J., Paul, B., Woodhead, J., Hergt, J., 2011. Iolite: Freeware for the visualisation and processing of mass spectrometric data. *J. Anal. At. Spectrom.* 26, 2508–2518.
- Patrick, R.A.D., Dorling, M., Polya, D.A., 1993. TEM study of indium- and copper-bearing growth-banded sphalerite. *Can. Mineral.* 31, 105–117.
- Qiu, W.J., Zhou, M.-F., Li, X., Williams-Jones, A.E., Yuan, H., 2018. The genesis of the giant Dajiangping SEDEX-Type Pyrite Deposit, South China. *Econ. Geol.* 113, 1419–1446.
- Rajabi, A., Canet, C., Rastad, E., Alfonso, P., 2015. Basin evolution and stratigraphic correlation of sedimentary-exhalative Zn-Pb deposits of the Early Cambrian Zarigan-Chahmir Basin, Central Iran. *Ore Geol. Rev.* 64, 328–353.
- Reed, M.H., Palandri, J., 2006. Sulfide mineral precipitation from hydrothermal fluids. *Rev. Mineral. Geochem.* 61, 609–631.
- Reich, M., Kesler, S.E., Utsunomiya, S., Palenik, C.S., Chryssoulis, S.L., Ewing, R.C., 2005. Solubility of gold in arsenian pyrite. *Geochim. Cosmochim. Acta* 69, 2781–2796.
- Sangster, D.F., 2002. The role of dense brines in the formation of vent-distal sedimentary-exhalative (SEDEX) lead-zinc deposits: field and laboratory evidence. *Miner. Deposita* 37, 149–157.
- Sangster, D.F., 2018. Toward an integrated genetic model for vent-distal SEDEX deposits. *Miner. Deposita* 53, 509–527.
- Schwartz, M.O., 2000. Cadmium in zinc deposits: *Econ. Geol. of a Polluting Element.* *Int. Geol. Rev.* 42, 445–469.

- Scott, S.D., 1983. Chemical behaviour of sphalerite and arsenopyrite in hydrothermal and metamorphic environments. *Mineral. Mag.* 47, 427–435.
- Seal, R.R., 2006. Sulfur isotope geochemistry of sulfide minerals. *Rev. Mineral. Geochem.* 61, 633–677.
- Seltmann, R., Shatov, V., Yakubchuk, A., 2013. Mineral deposits database and thematic maps of Central Asia, scale 1:1.5 million: ArcGIS 10.0, ArcView 3.2 and MapInfo 6.0 (7.0) GIS packages. Centre for Russian and Central Asian Mineral Studies, NHM London, p. 117.
- Sengör, A.M.C., Natalin, B.A., Burtman, V.S., 1993. Evolution of the Altaid tectonic collage and Paleozoic crustal growth in Eurasia. *Nature* 364, 299–307.
- Seward, T.M., Barnes, H.L., 1997. Metal transport by hydrothermal fluids. In: Barnes, H. L. (Ed.), *Geochemistry of Hydrothermal Ore Deposits*, third ed. John Wiley and Sons, New York, pp. 435–486.
- Shanks, W.C., 2001. Stable Isotopes in Seafloor Hydrothermal Systems: vent fluids, hydrothermal deposits, hydrothermal alteration, and microbial processes. *Rev. Mineral. Geochem.* 43, 469–525.
- Sherlock, R.L., Roth, T., Spooner, E.T.C., Bray, C.J., 1999. Origin of the Eskay Creek precious metal-rich volcanogenic massive sulfide deposit; fluid inclusion and stable isotope evidence. *Econ. Geol.* 94, 803–824.
- Sillitoe, R.H., Hannington, M.D., Thompson, J.F.H., 1996. High sulfidation deposits in the volcanogenic massive sulfide environment. *Econ. Geol.* 91, 204–212.
- Simmons, S.F., Brown, K.L., Tutolo, B.M., 2016. Hydrothermal Transport of Ag, Au, Cu, Pb, Te, Zn, and Other Metals and Metalloids in New Zealand Geothermal Systems: Spatial Patterns, Fluid-Mineral Equilibria, and Implications for Epithermal Mineralization. *Econ. Geol.* 111, 589–618.
- Slack, J.F., Dumoulin, J.A., Schmidt, J.M., Young, L.E., Rombach, C.S., 2004. Paleozoic sedimentary rocks in the Red Dog Zn-Pb-Ag district and vicinity, western Brooks Range, Alaska: provenance, deposition, and metallogenic significance. *Econ. Geol.* 99, 1385–1414.
- Song, X., 1984. Minor elements and ore genesis of the Fankou lead-zinc deposit, China. *Miner. Deposita* 19, 95–104.
- Steadman, J.A., Large, R.R., Olin, P.H., Danyushevsky, L.V., Meffre, S., Huston, D., Fabris, A., Lisitsin, V., Wells, T., 2021. Pyrite trace element behavior in magmatic-hydrothermal environments: An LA-ICPMS imaging study. *Ore Geol. Rev.* 128, 103878.
- Trofimova, L.A., Patalakha, G.B., Syromyatnikov, N.G., 1978. Track analysis of ores of the Tekeli deposit and its genetic significance. *Int. Geol. Rev.* 20, 1214–1220.
- Ulrich, T., Long, D.G.F., Kamber, B.S., Whitehouse, M.J., 2011. In situ trace element and sulfur isotope analysis of pyrite in a paleoproterozoic gold placer deposit, pardo and clement townships, Ontario, Canada. *Econ. Geol.* 106, 667–686.
- Wang, B., Liu, H., Shu, L., Jahn, B.-M., Chung, S.-L., Zhai, Y., Liu, D., 2014. Early Neoproterozoic crustal evolution in northern Yili Block: Insights from migmatite, orthogneiss and leucogranite of the Wenquan metamorphic complex in the NW Chinese Tianshan. *Precambrian Res.* 242, 58–81.
- Wei, C., Ye, L., Hu, Y., Danyushevskiy, L., Li, Z., Huang, Z., 2019. Distribution and occurrence of Ge and related trace elements in sphalerite from the Lehong carbonate-hosted Zn-Pb deposit, northeastern Yunnan, China: Insights from SEM and LA-ICP-MS studies. *Ore Geol. Rev.* 115, 103175.
- Wen, H., Zhu, C., Zhang, Y., Cloquet, C., Fan, H., Fu, S., 2016. Zn/Cd ratios and cadmium isotope evidence for the classification of lead-zinc deposits. *Sci. Rep.* 6, 25273–25273.
- Wilkinson, J.J., 2014. Sediment-hosted zinc-lead mineralization: processes and perspectives. In: Holland, H.D., Turekian, K.K. (Eds.), *Treatise on Geochemistry*, Second ed. Elsevier, Oxford, pp. 219–249.
- Windley, B.F., Alexeev, D., Xiao, W.J., Kröner, A., Badarch, G., 2007. Tectonic models for accretion of the Central Asian Orogenic Belt. *J. Geol. Soc.* 164, 31–47.
- Wohlgenuth-Ueberwasser, C.C., Viljoen, F., Petersen, S., Vorster, C., 2015. Distribution and solubility limits of trace elements in hydrothermal black smoker sulfides: An in situ LA-ICP-MS study. *Geochim. Cosmochim. Acta* 159, 16–41.
- Wright, K., Gale, J.D., 2010. A first principles study of the distribution of iron in sphalerite. *Geochim. Cosmochim. Acta* 74, 3514–3520.
- XBGM (Xinjiang Bureau of Geology and Mineral Resources), 1993. *Regional Geology of Xinjiang Uygur Autonomy Region*. Geology Publishing House, Beijing, pp.1–841 (in Chinese).
- Xiao, W.J., Han, C.M., Yuan, C., Sun, M., Lin, S.F., Chen, H.L., Li, Z.L., Li, J.L., Sun, S., 2008. Middle Cambrian to Permian subduction-related accretionary orogenesis of Northern Xinjiang, NW China: implications for the tectonic evolution of central Asia. *J. Asian Earth Sci.* 32, 102–117.
- Xie, Z., Xia, Y., Cline, J.S., Pribil, M.J., Koenig, A., Tan, Q., Wei, D., Wang, Z., Yan, J., 2018. Magmatic origin for sediment-hosted Au Deposits, Guizhou Province, China. In *Situ Chemistry and Sulfur Isotope Composition of Pyrites, Shuiyindong and Jinfeng Deposits*. *Econ. Geol.* 113, 1627–1652.
- Xue, C.J., Zhao, X.B., Mo, X.X., Chen, Y.C., Dong, L.H., Gu, X.X., Zhang, Z.C., Nurtaev, B., Pak, N., Li, Z.D., Wang, X.L., Zhang, G.Z., Yalikun, Y., Feng, B., Zu, B., Liu, J.Y., 2014. Tectonic-metallogenic evolution of western Tianshan giant Au-Cu-Zn-Pb metallogenic belt and prospecting orientation. *Acta Geol. Sin.* 88, 2490–2531 (in Chinese with English abstract).
- Xue, C.J., Zhao, X.B., Mo, X.X., Zu, B., Duan, S.G., Zhang, G.Z., Tan, H.D., Shao, X.L., Yalikun, Y., Man, R.H., Gao, R.Z., Zhang, Q., Feng, B., Chen, X., Liu, Y., Huang, P.X., Liu, C., Zhang, Y., 2017. Western Tianshan Cross-Border Metallogenic Belt. *Geology Publishing House, Beijing*, pp. 11–14 (in Chinese).
- Yakubchuk, A.S., Shatov, V.V., Kirwin, D., Edwards, A., Tomurtogoo, O., Badarch, G., Buryak, V.A., 2005. Gold and Base Metal Metallogeny of the Central Asian Orogenic Supercollage. *The 100th Anniv. Vol. of Econ. Geol.*, pp. 1035–1068.
- Ye, L., Cook, N.J., Ciobanu, C.L., Yuping, L., Qian, Z., Tiegeng, L., Wei, G., Yulong, Y., Danyushevskiy, L., 2011. Trace and minor elements in sphalerite from base metal deposits in South China: A LA-ICPMS study. *Ore Geol. Rev.* 39, 188–217.
- Yuan, H., Liu, X., Chen, L., Bao, Z., Chen, K., Zong, C., Li, X.-C., Qiu, J.W., 2018. Simultaneous measurement of sulfur and lead isotopes in sulfides using nanosecond laser ablation coupled with two multi-collector inductively coupled plasma mass spectrometers. *J. Asian Earth Sci.* 154, 386–396.
- Zhao, P.K., 2020. *Geology, geochemistry and genesis of the Tuokesai lead-zinc deposit, in the Western Tianshan Mountains, Xinjiang*. M.Sc. thesis, China University of Geosciences (Beijing), Beijing, China, 81 pp. (in Chinese with English abstract).
- Zhu, S.S., Cheng, Y., Yang, B., Zhang, J.L., Cao, X.N., Ai, L.J., Li, P., Zhang, H., Li, W.P., 2015. Detailed prospecting geological report of the Haerdaban Zn-Pb deposit, Wenquan, Xinjiang. Unpublished report, Xinjiang Institute of Geological Exploration for Nonferrous Resources, Urumqi, pp. 191 (in Chinese).